Winter 2012

Scale separation effects on mechanisms of boundary layer turbulence

Caleb Morrill Winter
University of New Hampshire, Durham

Scale separation effects on mechanisms of boundary layer turbulence

BY

Caleb Morrill Winter

B.S., Mechanical Engineering, University of New Hampshire, 2009

Submitted to the University of New Hampshire
in partial fulfillment of
the requirements for the degree of

Master of Science

in

Mechanical Engineering

December, 2012

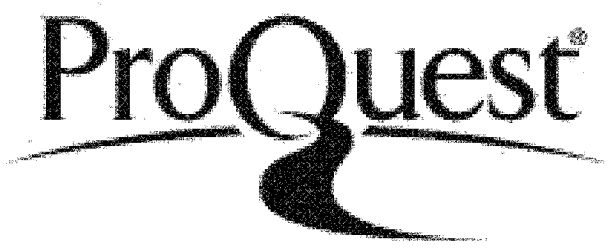

ProQuest LLC
789 East Eisenhower Parkway
P.O. Box 1346
Ann Arbor, MI 48106-1346

This thesis has been examined and approved.

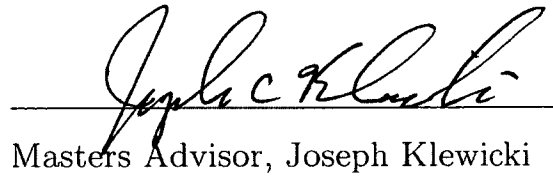

Masters Advisor, Joseph Klewicki

Professor of Mechanical Engineering

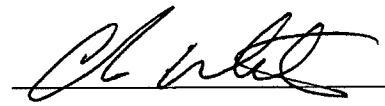

Christopher White

Associate Professor of Mechanical Engineering

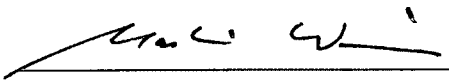

Martin Wosnik

Assistant Professor of Mechanical Engineering

12/04/2012

Date

DEDICATION

Dedication goes to my family.

ACKNOWLEDGMENTS

I wish to thank a number of people without whom this thesis would have been impossible.

Thanks to Paschal Vincenti, Rachel Ebner, Faraz Mehdi, Marc Bamberger and Naoufal Souitat.

TABLE OF CONTENTS

LIST OF TABLES

Table **Page**

LIST OF FIGURES

Figure **Page**

ABSTRACT

Scale separation effects on mechanisms of boundary layer turbulence

by

Caleb Morrill Winter

University of New Hampshire, December,, 2012

Correlations between specific velocity and vorticity components dictate how the distributions of mean momentum and turbulence kinetic energy are realized in the turbulent boundary layer. For turbulent inertia to remain dynamically significant at arbitrarily high Reynolds number, differences of these correlations must remain non-zero. This motivates the study of velocity vorticity products under the influence of increasing scale separation. Through the use of both laboratory and field data, scale separation between relevant velocity and vorticity components is shown to increase with distance from the wall and Reynolds number. Time-delayed correlations between the vertical velocity and spanwise vorticity fluctuations reveal that only very slight variations in their average phase relation would cause significant variations in the mean transport of momentum. Spectral analyses are used to explore previous observations of *scale selection* between the participating velocity and vorticity components. The wavelengths corresponding to the peaks in the relevant velocity and vorticity component spectra are used to describe scale separation effects. The variations in the wavelength ratios are shown to correlate with the scaling properties that

follow from the magnitude ordering of terms in the mean momentum equation. Scale separation is observed to arise via spatial confinement, and spatial dispersion. In the region where the mean viscous force is of leading order, the mechanism of vortex stretching generates motions bearing concentrated vorticity that, with increasing Reynolds number, are confined to a smaller fraction of the viscous region flow volume. In the region where the mean dynamics are inertially dominated, the characteristic vortical motions are sparsely dispersed over a domain whose thickness asymptotically grows like the boundary layer thickness. In the region $y^+ \lesssim 40$, the streamwise lengths of the correlations affiliated with turbulent inertia are seen to scale with the square root of the Reynolds number, while those affiliated with the gradient of turbulence kinetic energy are seen to scale with the Reynolds number itself.

CHAPTER 1

INTRODUCTION

Empirical observations, physical models, and theoretical results collectively lead one to surmise that wall-turbulence comprises a range of differently sized eddies that undergo sequences of similar characteristic interactions having essential features that are continually repeated [Marusic et al. (2010),Klewicki (2010)]. Consideration of net effects over time scales that are large compared to the integral scales of the turbulence leads one to further surmise that ensembles of these similarly recurring interactions are largely responsible for the observed properties of the mean-flow. Within this context, the mechanisms of present interest are those that underlie the net effect of the inertia of the turbulence on the establishment of the mean momentum field, as well as those interactions that underlie the establishment of the turbulence kinetic energy profile. For statistically stationary flows, the variables of interest are described by unclosed transport equations whose boundary conditions are at least partially known. Thus, the mechanisms describing the variation of these quantities between their boundary values are of primary concern.

Herein we explore the nature by which the velocity and vorticity fields interact to effect mean transport in turbulent wall-flows. Both theory and measurements indicate that the relative size difference (scale separation) between the largest and smallest motions in a turbulent flow increases with increasing Reynolds number. This phenomenon is generically reflected in the relative disparity between the integral length scale and the Kolmogorov microscale as the Reynolds number becomes large. Consistently, there is also an increasing disparity between the frequencies, wavenumbers,

or wavelengths that respectively characterize the primary contributions to the spectral intensities of the velocity and vorticity fluctuations. These are estimated, for example, by the wavelengths at which the relevant pre-multiplied spectra attain their maximum values.

This generic description has added complexity in the turbulent boundary layer. In wall-flows, the imposition of the wall boundary condition causes a spatial dependence in the size distribution of the dynamically significant motions, with the smaller motions exhibiting an increasing prevalence as $y \to 0$, where $y = 0$ denotes the plane of the wall. Thus, in the two-dimensional boundary layer the size distribution of the relevant motions varies as a function of both wall-normal position and Reynolds number. Little, however, is known about the relative size distribution of the characteristic vorticity and velocity field motions as δ^+ becomes large.

It is well-established that the dynamically important motions at least span the size range from the inner, $O(\nu/u_\tau)$, to the outer, $O(\delta)$, scales, where ν is the kinematic viscosity, $u_\tau = \sqrt{\tau_w/\rho}$ is the friction velocity (with τ_w and ρ the mean wall shear stress and mass density, respectively), and δ is the boundary layer thickness. The ratio of the outer length to inner length is given by

$$\delta^+ = \frac{\delta}{\nu/u_\tau}, \tag{1.1}$$

and thus the overall scale separation is directly reflected by the boundary layer Reynolds number. Herein we adopt the standard convention that a superscript + denotes normalization by inner variables.

Owing to considerations of both fundamental and technological importance, the study of Reynolds number dependence is a long-standing focus of turbulent boundary layer research. Many studies have revealed that the wall-normal profiles of the velocity fluctuation variances exhibit variations with increasing δ^+, [Klewicki (2010), Marusic

et al. (2010)] e.g., see Figs. 2-1a,b. Given this, we seek to better understand the mechanisms underlying the variation of the relevant profile in the wall-normal direction, y. These mechanisms are influenced by variations in δ^+ through their sensitivity to the increasing relative differences in the frequency or wavelength ranges of the velocity and vorticity field motions that determine their behaviors.

The issues just outlined motivate investigation of the influences of scale separation on the mechanisms associated with the net time-averaged effect(s) of turbulent inertia, as turbulent inertia drives the establishment of the mean momentum profile. Such considerations also motivate the similar study of the interactions that underlie the cross-stream variation of turbulence kinetic energy. Both of these are related to the difference of correlations between velocity and vorticity components, and thus these correlations are influenced by the increasing scale separation between their constituent components as δ^+ gets larger.

1.1 Relevant Velocity and Vorticity Field Interactions

Studies into the mechanisms by which the turbulence in the boundary layer establishes the distributions of mean momentum and turbulence kinetic energy are usefully guided by the tensor identity [Klewicki (1989a), Lele (1992), Eyink (2008)]

$$\frac{\partial \overline{u_j u_i}}{\partial x_j} = -\epsilon_{ijk}\overline{u_j \omega_k} + \frac{1}{2}\frac{\partial \overline{u_j u_j}}{\partial x_i}. \tag{1.2}$$

Setting $i = 1$ in (1.2) yields

$$\frac{\partial \overline{uv}}{\partial y} = \overline{w\omega_y} - \overline{v\omega_z} + \frac{1}{2}\frac{\partial(\overline{v^2} + \overline{w^2} - \overline{u^2})}{\partial x}. \tag{1.3}$$

Lower case letters denote zero-mean fluctuations (e.g., u, v and w, respectively denote the fluctuating streamwise, wall-normal and spanwise velocity components), upper case letters or an overbar (or angle bracket) signify mean quantities, and variants

of ω denote vorticity, with the component direction denoted by the subscript. In fully developed planar channel flow the streamwise gradient term in (1.3) is zero. For the two-dimensional boundary layer this term is non-zero but much smaller than the velocity vorticity terms, and becomes even smaller with increasing δ^+. Thus,

$$-\frac{\partial \overline{uv}}{\partial y} = \overline{v\omega_z} - \overline{w\omega_y} \tag{1.4}$$

holds to within the boundary layer approximation. As discussed further below, the difference of velocity vorticity correlations in (1.4) constitutes the mean effect of turbulent inertia in the differential statement of mean dynamics. Setting $i = 2$ in (1.2) and neglecting terms involving streamwise gradients yields

$$\frac{1}{2}\frac{\partial(\overline{u^2} + \overline{w^2} + \overline{v^2})}{\partial y} - \frac{\partial \overline{v^2}}{\partial y} = \overline{w\omega_x} - \overline{u\omega_z}, \tag{1.5}$$

or equivalently,

$$\frac{\partial q}{\partial y} - \frac{\partial \overline{v^2}}{\partial y} = \overline{w\omega_x} - \overline{u\omega_z}, \tag{1.6}$$

where q is the turbulence kinetic energy. Thus, the wall-normal variation of q is largely dictated by the difference of the velocity vorticity correlations appearing in (1.6).

The interactions between the velocity and vorticity components appearing in (1.4) and (1.6) are the central focus of the present investigation. Given this, a useful context is provided by describing the connections between the properties associated with the balance of terms in the mean momentum equation, the Reynolds number scalings affiliated with these properties, the theory that describes these properties, and observations that connect these properties to the development of the q profile.

1.2 Description of Mean Dynamics

For the flat plate turbulent boundary layer, the appropriately simplified form of the mean momentum equation contains three mechanistically distinct terms. The inertia of the mean flow (MI) and the mean effect of turbulent inertia (TI) appear on the left of (1.7), and the mean viscous force (VF) appears on the right. (Note that for consistency with previous publications we employ $T = -\rho\overline{uv}$.) In (1.7) the TI term is atypically positioned on the left. This is done to emphasize that it is not a stress divergence. Rather, it stems from the advective accelerations associated with a time-rate-of-change of momentum, and thus is more aptly described as the mean effect of turbulent inertia.

At each position within the boundary layer, the terms in (1.7) must balance. Not all terms, however, have leading order importance throughout the boundary layer. An understanding of the mean dynamics therefore requires a knowledge of the relative magnitudes or *magnitude ordering* of the terms at different positions across the layer. As first illustrated by Wei et al., [Wei et al. (2005)] the magnitude ordering of terms can be revealed by taking the ratio of the VF and TI terms. The resulting structure is schematically depicted in Fig. 1-1.

$$\rho\left(U\frac{\partial U}{\partial x}+V\frac{\partial U}{\partial y}\right)-\frac{\partial T}{\partial y}=\mu\frac{\partial^2 U}{\partial y^2} \tag{1.7}$$

Given (1.7), a non-trivial balance can only occur in the case of either two or three co-dominant terms. This balance is attained according to a different ordering in each of four layers: layer I, $|\mathrm{MI}| \simeq |\mathrm{VF}| \gg |\mathrm{TI}|$; layer II, $|\mathrm{VF}| \simeq |\mathrm{TI}| \gg |\mathrm{MI}|$; layer III $|\mathrm{MI}| \simeq |\mathrm{VF}| \simeq |\mathrm{TI}|$; layer IV, $|\mathrm{MI}| \simeq |\mathrm{TI}| \gg |\mathrm{VF}|$. The Reynolds number dependencies associated with the four layer regime are important to understanding the present analyses, and thus these are summarized in Table 1.1. The magnitude orderings associated with Fig. 1-1 reveal that for y values greater than the outer

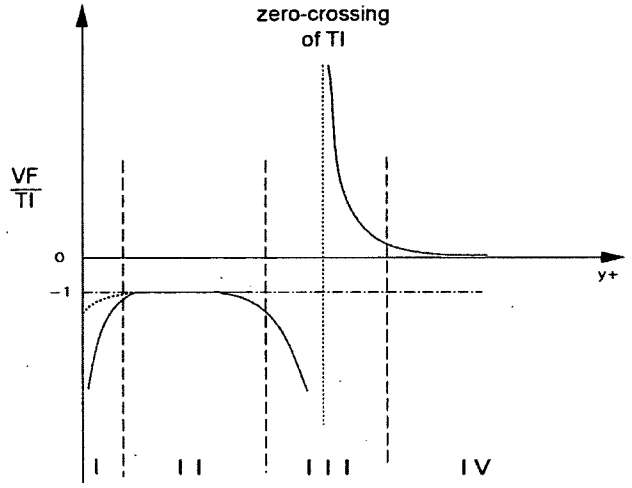

Figure 1-1. Sketch of the ratio of the mean viscous force (VF) to the mean effect of turbulent inertia (TI) in turbulent wall-bounded flows. Schematic is for a fixed Reynolds number. Note that layer I in the zero pressure gradient turbulent boundary layer (dotted line in layer I) is different from that of channel and pipe flow in that in this case all of the terms in the time averaged momentum equation approach zero as $y \to 0$.

edge of layer III the VF term is no longer dominant in (1.7). Consequently, for all y greater than this position the mean dynamics are dominated by the inertial terms. As indicated by the sketch of Fig. 1-1 and the scalings of Table 1.1, this position is located about $0.6\sqrt{\nu\delta/u_\tau}$ beyond the wall-normal position, y_m^+, where $T^+ = -\overline{uv}^+$ reaches its maximum value, or equivalently, the outer edge of layer III, which is located at $y^+ \simeq 2.6\sqrt{\delta^+}$ from the wall. Analysis, supported by existing empirical evidence indicates that this holds for all δ^+. Quantitatively, the scalings of Table 1.1 indicate that layer III is nominally *centered* about y_m^+. Numerous studies have shown $y_m^+ = \lambda\sqrt{\delta^+}$, with $\lambda \simeq 1.9$ [Long & Chen (1981), Afzal (1982), Sreenivasan & Sahay (1997), Wei et al. (2005)].

The four layer structure depicted in Fig. 1-1 also exists in fully developed pipe and channel flow. Boundary layer flows, however, exhibit significant differences in

Table 1.1. Scaling behaviors of the layer thicknesses and velocity increments associated with the mean momentum equation, see Fig. 1-1. Note that the layer IV properties are asymptotically attained as $\delta^+ \to \infty$. Note also that existing evidence indicates that layer I is thinner in boundary layers than in pipes or channels. Thus, its thickness and velocity increment are both indicated to be $\lesssim 3$.

Physical layer	Δy increment	ΔU increment
I	$O(\nu/u_\tau)$ $(\lesssim 3)$	$O(u_\tau)$ $(\lesssim 3)$
II	$O(\sqrt{\nu\delta/u_\tau})$ $(\simeq 1.6)$	$O(U_\infty)$ $(\simeq 0.5)$
III	$O(\sqrt{\nu\delta/u_\tau})$ $(\simeq 1.0)$	$O(u_\tau)$ $(\simeq 1)$
IV	$O(\delta)$ $(\to 1)$	$O(U_\infty)$ $(\to 0.5)$

the way this structure emerges at low δ^+. For example, the four layer regime is first realized at $\delta^+ \simeq 180$ in fully developed pipe and channel flows, but is not established until $\delta^+ \simeq 360$ in the flat plate boundary layer [Elsnab et al. (2011), Klewicki et al. (2011), Klewicki et al. (2012)]. The magnitude ordering of terms associated with the four layer regime exists for all higher δ^+, and these relative magnitudes become more disparate as $\delta^+ \to \infty$. As a consequence, the scaling behaviors associated with this regime are more definitively realized as $\delta^+ \to \infty$ [Fife et al. (2009)].

TI passes through zero at y_m^+ and thus, if interpreted as a force, this term acts like a momentum source for $y^+ < y_m^+$ and a momentum sink for $y^+ > y_m^+$ [Klewicki et al. (2007)]. The positions of the peak values of the TI profile (inner positive at y_{pi}, outer negative at y_{po}) have been shown to bound a continuous hierarchy of scaling layers [Fife et al. (2005)]. Collectively, this hierarchy of layers is called the L_β hierarchy. The defining attribute of the L_β hierarchy is that from layer-to-layer the mean dynamics attain approximate self-similarity at any finite δ^+, and approach exact self-similarity as $\delta^+ \to \infty$. This attribute stems from the fact that on each of the layers (1.7) formally admits the same invariant form. At any given wall-normal location, this invariant form is attained by employing the local width, $W(y^+)$, of the L_β layer on the hierarchy [Fife et al. (2009)].

Self-similar mean dynamics are attained on the hierarchy as a function of scale. Physically, this self-similarity reflects how the differing scales of motion, on average, cause a *balance breaking and exchange* of forces across each layer of the hierarchy. This is clarified by recognizing that layer III in Fig. 1-1 results from the ensemble average of all of the layers on the hierarchy. As a result, layer III is centered about the geometric mean of the upper and lower bounds of the hierarchy, and the width of layer III is the geometric mean of the minimum and maximum $W(y^+)$ values [Klewicki et al. (2011)]. Layer III is therefore precisely identified as the L_β layer centered about y_m^+, e.g., see refs. 11 and 15. Fig. 1-1 shows that the balance breaking and exchange of mean forces across layer III is associated with the VF term losing leading order importance from layer II to layer IV. On average, this same process occurs as a function of scale across every layer on the hierarchy [Fife et al. (2009)].

The properties of the L_β hierarchy are indicative of approximately self-similar behaviors in the slope and curvature of the $T^+(y^+)$ profile, with the accuracy of the approximation improving as $\delta^+ \to \infty$ [Fife et al. (2005), Fife et al. (2009)]. The position of the L_β hierarchy relative to the properties of the T^+ and $\partial T^+/\partial y^+$ profiles is shown for a low δ^+ boundary layer in Fig. 1-2. As indicated, the inner peak in the TI profile (inflection in T^+ from upward to downward curvature) is located at $y_{pi}^+ \simeq 7$, and the outer peak in the TI profile (inflection in T^+ from downward to upward curvature) is located at $y_{po}/\delta \simeq 0.5$.

A primary property of the L_β hierarchy is its inner-normalized layer width distribution, $W(y^+)$. For turbulent wall-flows in general, $W(y^+)$ is given by the order of magnitude estimate,

$$W(y^+) = O(\beta^{-1/2}), \tag{1.8}$$

where β is a small parameter related to the decay rate of TI [Fife et al. (2005)]. The parameter β is used to transform T^+. This allows the mean dynamical equation to be written in a single invariant form on each L_β layer, and exposes the scale-dependencies underlying the self-similar dynamics on the hierarchy [Fife et al. (2009)]. For the boundary layer, the balance of (1.7) dictates that the estimate for the parameter β is influenced by the mean inertia profile, which is a non-simple function of δ^+ and y^+ [Klewicki et al. (2011)]. This is distinct from the pipe or channel, since in these cases the analogous inner-normalized pressure gradient term has a constant magnitude that is directly proportional to δ^+. For a sub-domain on the hierarchy, $W(y^+)$ asymptotically scales linearly with distance from the wall, i.e., $dW/dy^+ =$ A/2 = constant. Thus, this attribute of the overall theory constitutes a well-founded explanation for why the often assumed *distance from the wall* scaling is operative [Fife et al. (2005), Fife et al. (2009), Klewicki et al. (2009)]. Over the part of the hierarchy closer to the wall, existing evidence suggests that $W(y^+)$ is a universal function of y^+.

The structure shown in Fig. 1-2 has significance relative to describing Reynolds number dependences, and the attendant scale separation. Namely, transitional regime data provide evidence that the hierarchical structure comes into being via the spread of turbulent inertia from an interior zone toward the periphery of the flow, i.e., simultaneously toward the wall and the freestream. As a consequence, the inner and outer lengths of (1.1) attain relevance to scaling boundary layer statistics only after the smallest and largest length scales of the hierarchy (W_{min} and W_{max}, respectively) become constrained by the boundary conditions [Klewicki et al. (2011)]. Increases in Reynolds number are then marked by the broadening of the hierarchy such that it always spans the length scale range from $O(\nu/u_\tau)$ to $O(\delta)$. With increasing δ^+ the

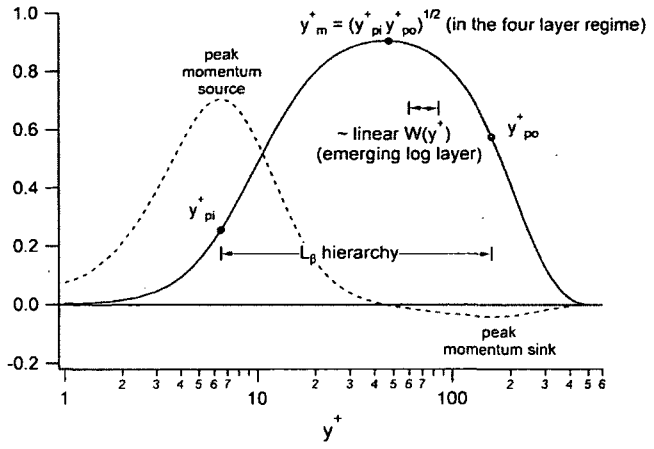

Figure 1-2. Position of the L_β hierarchy in relation to the profiles of $-\overline{uv}^+$ (solid line) and $-\partial\overline{uv}^+/\partial y^+$ (dashed line). Note that the Reynolds stress gradient profile is multiplied by a factor of ten for clarity. Data are from the $\delta^+ = 367$ boundary layer of Wu and Moin [Wu and Moin (2009)]. Figure is adapted from Klewicki et al. [Klewicki et al. (2011)].

dynamics on an interior domain become increasingly independent of the boundary constraints.

The theoretical description just given is distinct from ones that attach the dynamics of the interior domain to inner and outer functions that, for all δ^+, are taken to be simultaneously valid (overlap) on the interior domain [Fife et al. (2009)]. On the other hand, the expanding layer hierarchy affiliated with increasing δ^+ exhibits remarkable consistency with phenomenologies originating from Townsend's attached-eddy description of wall-turbulence [Townsend (1976), Perry & Chong (1982), Perry & Marusic (1995)].

1.3 Turbulence Kinetic Energy Considerations

The analysis methods used to determine the properties of (1.7) outlined above are not as easily applied to the problem of the turbulence kinetic energy distribution. This is because the underlying transport equation describing $q^+(y^+)$ is more complex

than (1.7). A number of empirical studies, however, provide insights regarding the factors influencing the properties of the $q^+(y^+)$ profile (e.g., see ref. 1 and the references therein). Owing at least partly to the simplicity of its measurement, much attention has been paid to quantifying the δ^+ dependence of $\overline{u^2}^+$. This quantity is the dominant contributor to q^+, and its transport equation contains the primary turbulence production term that also appears in the transport equation for q^+. Evidence from well-resolved laboratory and field data indicates that the near-wall peak in the boundary layer $\overline{u^2}^+$ profile (located near $y^+ = 15$) increases with increasing δ^+ [Klewicki (2010)]. While a logarithmic fit of existing $\sqrt{\overline{u^2}^+}$ data convincingly reveals a δ^+ dependence, [Metzger & Klewicki (2001)] a logarithmic fit of $\overline{u^2}^+$ itself does so as well, while also finding phenomenological support via the attached-eddy model [Perry & Chong (1982), Perry & Marusic (1995)]. Empirical analyses suggest that the δ^+ dependence in the vicinity of the near-wall profile peak can be removed by using the mixed normalization $\overline{u^2}^+/(U_\infty u_\tau)$ [DeGraaff & Eaton (2000)]. A cogent theoretical explanation for this observation has, however, yet to be fully formulated.

Farther away from the wall, there is some evidence (including the $\delta^+ \simeq 8.9 \times 10^5$ data herein) that a so-called *outer peak* appears in the boundary layer $\overline{u^2}^+$ profile. Data scatter and sensor resolution effects, however, render definitive conclusions premature. Whether or not there emerges an outer peak in the $\overline{u^2}^+$ profile, there is compelling evidence that, with increasing δ^+, the underlying spectrum develops a peak much farther from the wall than the $y^+ \simeq 15$ position of the spectral peak affiliated with the near-wall maximum of $\overline{u^2}^+$. The streamwise wavelength of this "outer peak" is observed to be as large as about 6δ [Hutchins & Marusic (2007)].

The position of this spectral peak and the associated physics appear to correlate with the structure of Fig. 1-1, as well as the underlying L_β layer hierarchy. For

example, the position where this peak is most prominent is well-approximated by the equation

$$y^+_{peak} = B\sqrt{\delta^+}, \tag{1.9}$$

with $B \simeq 3$. Similarly, recent evidence indicates that the meandering "superstructures" found in the region where the mean profile is logarithmic have a clear modulating influence on the smaller scale energetic motions near the wall [Mathis et al. (2009a), Mathis et al. (2009b)]. The analysis of Mathis et al [Mathis et al. (2009a)]. indicates that the zero-crossing of the modulation correlation coefficient occurs near the center of the logarithmic layer, $y^+ \simeq \sqrt{15\delta^+} \simeq 3.9\sqrt{\delta^+}$, if one assumes that, independent of δ^+, the logarithmic layer extends from $y^+ \simeq 100$ to $y/\delta \simeq 0.15$.

There are reasons to consider refinements to this estimate. A fit of the data that Mathis et al. present is well-approximated by (1.9), but with $B \simeq 3.1$. Recent empirical evidence and the analyses associated with section 1.2 indicate that the lower bound of the region where a logarithmic mean profile first appears moves outward in y^+ units with increasing δ^+ [Wei et al. (2005), Nagib et al. (2007), Fife et al. (2009)]. According to this theory, logarithmic behavior (approximate or exact) is attained when $W(y^+)$ becomes linear (approximately or exactly). With increasing (post-transitional) Reynolds number, this condition is first attained on an interior sub-domain of the L_β layer hierarchy. This sub-domain starts near the outer edge of layer III ($y^+ \simeq 2.6\sqrt{\delta^+}$), and ends interior to the upper bound of the hierarchy ($y/\delta \simeq 0.5$) [Klewicki et al. (2009), Elsnab et al. (2011), Klewicki et al. (2011), Klewicki et al. (2012)]. Figure 1-2 shows that the extent of this sub-domain is small at low δ^+. Physically, this sub-domain of the hierarchy is where the mean dynamics are dominated by the inertial mechanisms in (1.7), and thus its existence is consonant with the classical notion of the logarithmic layer constituting an inertial sublayer in physical

space [Tennekes & Lumley (1972), Klewicki et al. (2007)]. This theoretically based prescription for the onset of the logarithmic layer has intriguing consistency with the recent support for the prediction of Townsend that, with increasing δ^+, a logarithmic dependence in the $\overline{u^2}^+$ profile emerges over the same spatial domain where the U^+ profile also best approximates a logarithmic function [Smits et al. (2011)]. Thus, in contrast to being located at the *center* of the logarithmic layer, these analyses identify the modulation zero-crossing with the lowest portion of the inertial layer where a logarithmic $U^+(y^+)$ first emerges.

A description of the so-called inner/outer interaction that is founded in the analysis of (1.7) also has apparent correlation with the superstructure modulation of shear stress fluctuations. The dynamical structure of Fig. 1-1 leads one to surmise that, on average, the inner/outer interaction occurs across layer III, with the inertially dominated motions in layer IV communicating with the highly vortical motions in layer II [Klewicki et al. (2007)]. Experiments at $\delta^+ = 12424$ that measured the streamwise velocity profile conditioned on the presence of low frequency negative and positive wall shear stress fluctuations indicate that the conditional mean profiles at zero time delay exhibit maximal excursion from the long-time mean profile at $y^+/\sqrt{\delta^+} \simeq 2.6$, while the correlation with the conditional criteria (based upon the fluctuating wall shear stress), is lost for $y/\delta \gtrsim 0.5$ [Hutchins et al. (2011)]. An annotated version of their result is shown in Fig. 1-3. As described above, the positions $y^+/\sqrt{\delta^+} \simeq 2.6$ and $y/\delta \simeq 0.5$ bound the sub-domain on the L_β hierarchy where a logarithmic $U^+(y^+)$ first emerges. Physically, the results of Fig. 1-3 suggest that the inertial eddies (superstructures) in the lowest portion of layer IV modulate a local equilibrium flow for $y/\sqrt{\nu\delta/u_\tau} \lesssim 2.6$. Collectively, these and the above observations motivate examination of the present data relative to the layer boundaries of Fig. 1-1, as well as other features affiliated with the L_β hierarchy.

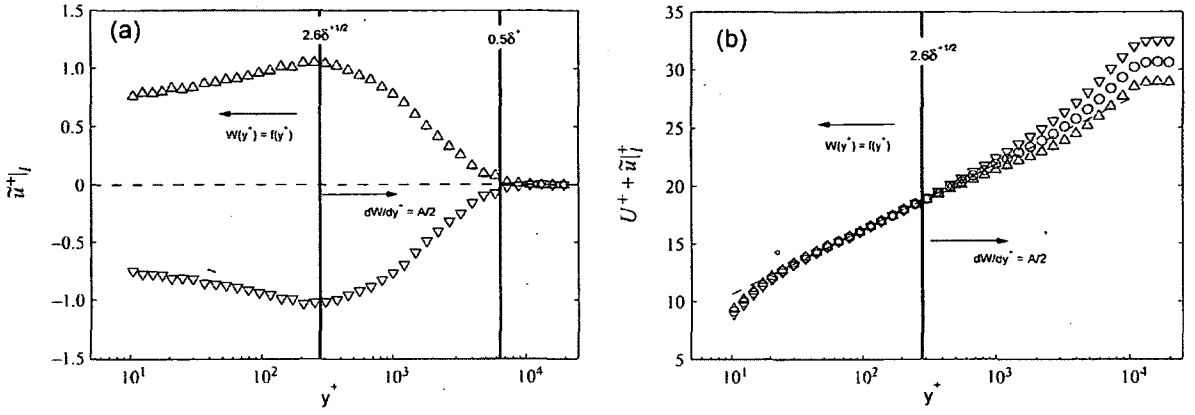

Figure 1-3. Properties of the streamwise velocity profiles conditioned on high (triangle up) and low (triagle down) wall shear stress events (circles show the long time mean) at $\delta^+ = 12424$: (a) difference between the conditional and mean profiles, (b) conditional profiles normalized by the conditional u_τ. Adapted from Hutchins et al. [Hutchins et al. (2011)]. For consistency with other studies, their estimate for δ^+ has been converted to δ^+_{99}.

1.4 Characteristic Interactions

Equation 1.2 has use in the study of Reynolds number dependence. All reliable evidence indicates that the mechanism of turbulent inertia in (1.7) is not only important at any given (post-transitional) δ^+, but increases in significance as $\delta^+ \to \infty$. On the other hand, (1.4) broadly indicates that the efficacy of this mechanism is dictated by a nonzero difference of correlations in (1.3) and (1.5) as $\delta^+ \to \infty$. Thus, questions arise regarding how this occurs as the wavelengths characteristic of the contributing velocity and vorticity components become increasingly dissimilar.

Characteristic spectral interactions are clarified by considering the sketch of Fig. 1-4. In this figure, the pre-multiplied spectra of the pertinent velocity and vorticity components are represented by Ψ_u and Ψ_ω, respectively. For the present analyses, the peak in any given spectrum is used to nominally identify the characteristic frequency or wavelength. One way to quantify the net scale separation is the wavelength difference between the peak values of Ψ_u and Ψ_ω. A second way is to form the ratio, λ_u/λ_ω, where λ_u and λ_ω respectively denote the wavelengths at the spectral peaks.

Under the condition $\lambda_u \gg \lambda_\omega$ (say greater than about one decade) their difference approaches a constant value, $\simeq \lambda_u$. Their ratio, however, continues to proportionally reveal increasing scale separation. For this reason, the analyses herein employ the wavelength ratio.

Two different pre-multiplied co-spectra are also depicted in Fig. 1-4. Recall that the wavelength integral of the co-spectrum is equal to the correlation between the two variables. For the indicated scale separation, it is rational to expect the associated pre-multiplied co-spectrum to predominantly concentrate in a wavelength range common to the participating velocity and vorticity components. This expectation, depicted by the pre-multiplied co-spectra, Λ_1, follows from the notion that the most vigorous interactions occur between motions having similar characteristic wavelengths. Priyadarshana et al [Priyadarshana et al. (2007)]. provide evidence, however, that the net correlation is often (perhaps generically) produced by a *scale selection* concentrated in a wavelength range near the peak of Ψ_u or Ψ_ω, or both. Thus, for example, the sketch of Λ_2 depicts a scale selection associated with the dominant wavelengths of Ψ_u and Ψ_ω. The increasing scale separation with increasing y^+ and δ^+ discussed above motivates investigation of scale selection sensitivities to both distance from the wall and Reynolds number.

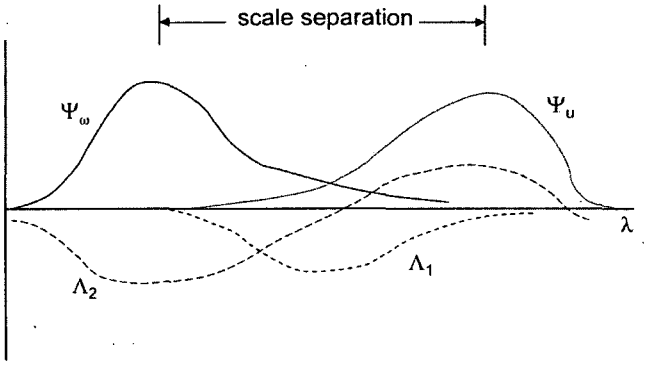

Figure 1-4. Sketches of the pre-multiplied wavelength spectra representative of velocity and vorticity components, Ψ_u and Ψ_ω, respectively. Λ_1 exemplifies a co-spectrum associated with interactions primarily involving the wavelength range shared by Ψ_u and Ψ_ω. Λ_2 exemplifies a co-spectrum associated with interactions resulting from *scale selections* occurring in wavelength ranges centered about the peak values of Ψ_u and Ψ_ω.

CHAPTER 2

EXPERIMENTAL CONSIDERATIONS

2.1 Data Sets Employed

The present study utilizes low Reynolds number data from well-resolved laboratory measurements over the range $375 \lesssim \delta^+ \lesssim 1,500$. These are supplemented with high Reynolds number data ($\delta^+ \simeq 8.9 \times 10^5$) that were acquired under near-neutral thermal stratification in the atmospheric surface layer that flows over the salt playa at the Surface Layer Turbulence and Environmental Science Test (SLTEST) facility in western Utah [Klewicki et al. (1995), Klewicki et al. (1998), Metzger & Klewicki (2001)]. The laboratory data are derived from four-element hotwire sensor measurements acquired in a low speed, zero pressure gradient, boundary layer flow that developed over fetch of about a 16m [Klewicki (1989a), Klewicki & Falco (1990), Klewicki & Falco (1996)]. The field data were acquired using a six-element hotwire sensor described in the studies by Priyadarshana et al. [Priyadarshana & Klewicki (2004), Priyadarshana et al. (2007)]. In both cases, the sensors provided time-resolved measurements of the streamwise and wall-normal velocity components ($\tilde{u} = U + u$ and $\tilde{v} = V + v$, respectively), along with the spanwise (z) component of the fluctuating vorticity, $\omega_z = \partial v/\partial x - \partial u/\partial y$.

A summary of the experiment parameters is given in Table 2.1. The low Reynolds number measurements span wall-normal locations from $y^+ \simeq 5$, to $y/\delta \simeq 1$. The high Reynolds number data span the domain $200 \lesssim y^+ \lesssim 4,000$, and thus this only covers a very small fraction of the overall flow width ($0.00023 \lesssim y/\delta \lesssim 0.0045$).

Relative to the layer scalings of Table 1.1, however, the range is $0.21 \lesssim y/\sqrt{\nu\delta/u_\tau} \lesssim 4.25$, which is significant since it begins in the middle of layer II and ends in the lowest portion of layer IV. As indicated, the low δ^+ experiments were conducted over an aerodynamically smooth surface, while the high δ^+ data were acquired over a surface having an equivalent sand grain roughness of $25 \lesssim k^+ \lesssim 50$ [Priyadarshana & Klewicki (2004)]. Based upon comparisons with data having similar and much larger k^+ values at both high and low δ^+, one can safely conclude that the observed differences between the present high and low δ^+ data almost entirely result from Reynolds number effects; with any roughness influences embedded within the high δ^+ data scatter [Priyadarshana et al. (2007)].

The low δ^+ measurements are normalized with a friction velocity estimated from a Clauser plot, while at high δ^+ u_τ was found using a 2.4m diameter floating-element drag plate [Klewicki & Falco (1990), Sadr & Klewicki (2000)]. Turbulence measurements, and especially those affiliated with velocity gradients, are sensitive to spatial and temporal resolution effects [Johansson & Alfredsson (1983), Klewicki & Falco (1990), Antonia et al. (1993), Hutchins et al. (2009)]. Since the present measurements were all acquired at low speeds ($U \leq 5$m/s), the frequency content of the signals never exceeded 4kHz. Thus, the temporal resolution requirements were readily met by the constant temperature anemometry circuits and data acquisition equipment [Klewicki & Falco (1990), Priyadarshana & Klewicki (2004)]. Similarly, the l^+ entries in Table 2.1 indicate that the sensor spatial resolution pertaining to the u and v measurements was also very good – ranging between $l^+ = 2$ at $\delta^+ = 375$ to $l^+ = 11$ at $\delta^+ \simeq 8.9 \times 10^5$. As demonstrated in Figs. 2-1a,b, the present inner-normalized streamwise and wall-normal velocity intensities exhibit Reynolds number trends that are known to become apparent when sensors of sufficient spatial resolution are employed [Klewicki (2010)]. Examples of these include the increasing near-wall peak in the u'^+ profile with in-

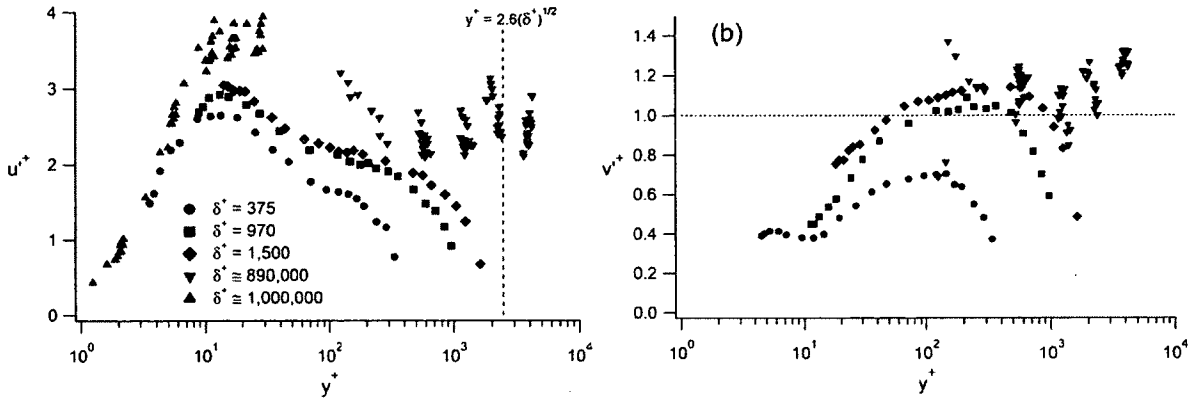

Figure 2-1. Inner-normalized velocity intensities of the present study, (a) streamwise intensities, (b) wall-normal intensities. Near-wall u'^+ data at $\delta^+ \simeq 1 \times 10^6$ are from the study of Metzger and Klewicki [Metzger & Klewicki (2001)].

creasing δ^+, as well as the broader extent of the plateau about the maximum in the v'^+profile. At high Reynolds number the present u'^+ profile exhibits a hint of an outer peak located near $y^+ = 2,400$, or equivalently $y^+/\sqrt{\delta^+} = 2.55$. In connection with these data, it has also been previously shown that the increasing u'^+ and v'^+ values underlie an approximately logarithmic reduction in the correlation coefficient, $\overline{uv}/u'v'$, with increasing δ^+ [Priyadarshana & Klewicki (2004)].

The sensor spacing in the four-element probe, Δy^+, associated with the estimation of $\partial u/\partial y$ is also equal to l^+. From low Reynolds number wind tunnel experiments it is expected that a $\Delta y^+ = 7.2$ spacing will cause an attenuation of less than 5% when compared to a sensor with a spacing of $\Delta y^+ = 2.0$ [Klewicki & Falco (1990)]. Folz and Wallace studied this issue relative to measurements in the atmospheric surface layer [Folz & Wallace (2009)]. They found that a wire spacing of about $2\pi\eta$ (where $\eta = (\nu^3/\epsilon)^{1/4}$ is the Kolmogoroff microscale, and ϵ is the turbulence dissipation rate) yields minimal derivative signal attenuation, and simultaneously minimizes the adverse effects of signal noise [Klewicki & Falco (1990), Antonia et al. (1993)]. In the six-element sensor $\Delta y^+ \simeq 3l^+ \simeq 33$. Based upon the η estimates

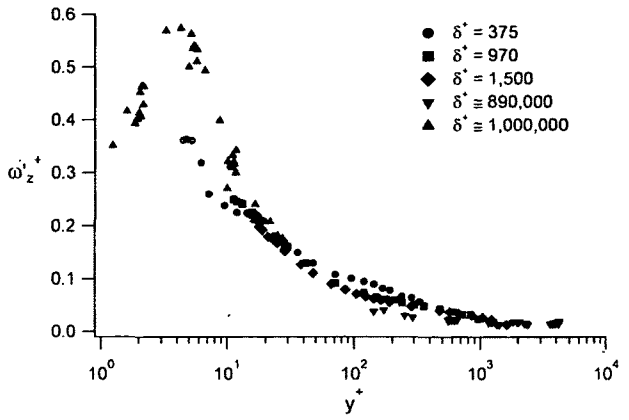

Figure 2-2. Inner-normalized spanwise vorticity intensities from the data sets employed in the present study, as well as the inner-normalized near-wall $\partial u/\partial y$ intensities at $\delta^+ \simeq 1 \times 10^6$ from the study of Metzger and Klewicki [Metzger & Klewicki (2001)].

Table 2.1. Parameters associated with the present experimental data sets. Note that average values are given for the $\delta^+ = 8.9 \times 10^5$ data set, while analyses of the individual signals used the u_τ value affiliated with that signal.

δ^+	u_τ (m/s)	ν m^2/s	k^+	l^+	Δy^+
375	0.0282	1.50×10^{-5}	Smooth	2.0	2.0
970	0.0707	1.50×10^{-5}	Smooth	4.3	4.3
1,500	0.1125	1.50×10^{-5}	Smooth	7.2	7.2
8.9×10^5	0.1962	1.85×10^{-5}	$25-50$	11	33

of Priyadarshana et al., [Priyadarshana et al. (2007)] this spacing ranged between $4 \lesssim \Delta y/\eta \lesssim 13$, or equivalently between about 0.6 and 2.2 times the criteria given by Folz and Wallace. Thus, the instantaneous $\partial u/\partial y$ signals derived from this sensor are expected to exhibit some attenuation, especially for positions closer to the wall. This expectation is supported by Fig. 2-2, which shows that the $\delta^+ \simeq 8.9 \times 10^5$ data are detectably below the laboratory profiles for $y^+ \lesssim 300$.

2.2 Spectral Analysis

Spectral representations and measurements are employed throughout the following data analysis. The premultiplied spectra and cospectra presented herein were computed using methods similar to those described by Priyadarshan and Klewicki [Priyadarshana & Klewicki (2004)]. The signal was divided into windows prior to computing the Fast Fourier Transform (FFT). The durations of the FFT windows, as quantified in viscous time scales were 154.1, 154.9, 196.2, and 143.6 for $\delta^+ = 375$, 970, 1500, and $\simeq 8.9 \times 10^5$, respectively. The Welch averaging method was used. This method splits the data into overlapping segments of the signal windowing size, computes periodograms of the segments, and then ensemble averages the periodograms to get the spectral estimate. A Hamming window equal the signal-window was used to reduce spectral leakage. A Savitzky-Golay smoothing filter was employed in order to better estimate the wavelengths associated with the peaks in the pre-multiplied spectra. Visual inspections verified that these smoothed spectra faithfully tracked the un-smoothed spectra. The Savitzky-Golay filtering window ranged between $0.05-0.21$ viscous time scales, depending on the wall-normal position and Reynolds number, and a quadratic fit was used as the smoothing polynomial. The spectra and cospectra were normalized by their respective variances. A third order polynomial regression fit to the spectra was made in the vicinity of the spectral peak. This curve-fit extended over those wavelengths corresponding to spectral values that exceeded an 85% threshold of the maximum spectral value. The wavelength corresponding to the location of the spectral peak value was then estimated by the location where slope of the fit was zero. In the scale-selection analysis down-sampling of between $3 - 21$ times less than the sampling frequency was used to better resolve spectral curvature at large wavelengths. Down-sampling was preferred over a more extreme Savitzky-Golay filtering window because it did not produce any identifiable distortion to the spectra.

CHAPTER 3

RESULTS

The following data presentation first explores the spatial structure of the relevant velocity and vorticity component interactions. The properties of the velocity and vorticity spectra and their associated co-spectra are then analyzed to clarify the effects of the scale selection and scale separation phenomena discussed above.

3.1 Correlation Structure

3.1.1 Zero Lag Correlation Profiles

A useful context is established by first presenting the inner-normalized profiles of the zero time-delay correlations between v and ω_z and u and ω_z. These profiles, some of which have been presented in previous publications, [Klewicki (1989a), Priyadarshana et al. (2007)] are shown in Figs. 3-1a,b, respectively.

The low $\delta^+ \overline{v\omega}_z^+$ correlations of Fig. 3-1a are positive interior to $y^+ \lesssim 15$, but then display negative values for all greater y^+ positions in the boundary layer. Measurements by Ragagopalan and Antonia at $\delta^+ \simeq 500$ are consistent with these, including the observed Reynolds number dependence [Ragagopaln & Antonia (1993)]. The profiles of Fig. 3-1a exhibit a clear δ^+ dependence for $y^+ > 20$. Namely, the maximum magnitude of the negative portion is a strongly decreasing function of Reynolds number, with the position of the maximum peak apparently moving outward with δ^+. A study of the evolution of the balance expressed by the mean momentum equation through the transitional regime reveals that, prior to and early within the four layer

regime, the TI and MI terms in (1.7) are rapidly changing functions of δ^+ in the outer region [Klewicki et al. (2011)]. (Recall that the $\delta^+ = 375$ flow is barely within the four layer regime.) These changes are affiliated with the diminishing influence of the VF term, and the establishment of TI and MI as the two dominant terms in layer IV.

Equation 1.3 connects these observed changes to the $\overline{v\omega}_z^+$ profiles of Fig. 3-1a. Relative to the structure of the L_β layer width distribution, $W(y^+)$, it also is potentially significant to note that the negative peak in each of the low δ^+ profiles of Fig. 3-1a approximately corresponds with the position of W_{max}, $y/\delta \simeq 0.5$. Unlike the profile at $\delta^+ = 375$, however, those at $\delta^+ = 970$ and $1,500$ also have a different shape in the interior of the flow – exhibiting a subtle peak that apparently moves outward with Reynolds number at a rate intermediate to inner and outer scaling. At $\delta^+ = 375$ there is minimal scale separation. Therefore, the features exhibited by the higher δ^+ laboratory data are affiliated with a fuller realization of the L_β hierarchy. (Recall that, for any given δ^+, $W(y^+)$ spans $O(\nu/u_\tau)$ to $O(\delta)$ over a domain that spans $O(\nu/u_\tau)$ to $O(\delta)$.) Furthermore, by recalling that the $\delta^+ \simeq 8.9 \times 10^5$ data are nominally centered about y_m^+, it becomes apparent that the shape of the profile segment described by these data is also consistent with the trend exhibited by the $\delta^+ = 970$ and $1,500$ profiles in the vicinity of their respective y_m^+. Regarding these data, note that a sign error was discovered since there original presentation, and thus their ensemble averaged representations in Priyadarshana et al. [Priyadarshana et al. (2007)] have the opposite sign.

The most distinctive feature of the $\overline{u\omega}_z^+$ profiles of Fig. 3-1b is the negative peak value near the edge of layer I ($y^+ \simeq 5$). This peak attains a magnitude of approximately 0.65, which is about ten times larger than the positive near-wall peak displayed by the $\overline{v\omega}_z^+$ profile of Fig. 3-1a. The physical reason for this peak is the increasingly perfect anti-correlation between $u(t)$ and $\omega_z(t)$ as the no-slip wall at $y^+ = 0$ is ap-

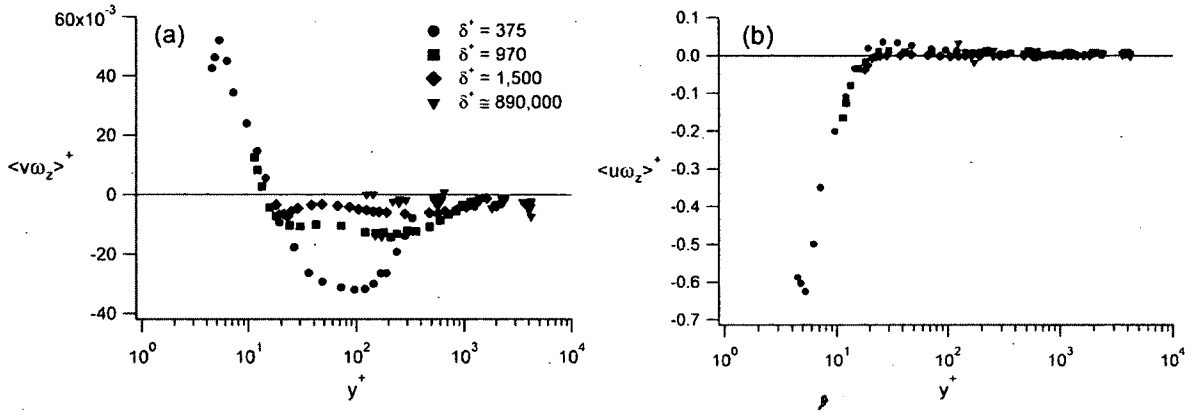

Figure 3-1. Inner-normalized profiles of the zero time-delay correlation between, (a) v and ω_z, and (b) u and ω_z.

proached [Klewicki (1989a)]. Examination of the corresponding correlation coefficient, $\overline{v\omega}_z/u'\omega'_z$, indicates a very similar profile shape, except that it continues to approach -1 as $y^+ \to 0$ [Klewicki (1989b),Ragagopaln & Antonia (1993)]. Equation 1.5 reveals that this highly negative correlation largely underlies the rapid near-wall rise in q; thus indicating that this feature of wall-turbulence is an essentially unavoidable consequence of the constraints imposed on the velocity and vorticity fields by a no-slip wall [Klewicki (1998)].

The profiles pass through zero at $y^+ \simeq 15$, i.e., near the peak in u'^+. For greater y^+, close examination reveals that all of the profiles exhibit slightly positive values. (The bulk of the $\delta^+ \simeq 8.9 \times 10^5$ data are positive, but with a few of the points in the ensemble falling below zero.) While, these positive values are small relative to the large negative peak near the wall, they are of the same order of the outer region $\overline{v\omega}_z^+$ data of Fig. 3-1a [Klewicki (1989a)]. Their physical significance is revealed by (1.5), indicating that the decay of q (negative $\partial q/\partial y$) is effectively determined by the difference, $\overline{w\omega}_x^+ - \overline{u\omega}_z^+$. It thus becomes apparent that the physics determining the existence (or nonexistence) of the so-called "outer peak" in the $q(y^+)$ profile are embodied in the velocity and vorticity field interactions underlying these correlations.

In this regard, note that the laboratory $\overline{u\omega_z}^+$ profiles exhibit a δ^+ dependence beyond $y^+ \simeq 15$.

3.1.2 Streamwise Correlation Structure

As discussed in section 1.2, the length scale distribution (layer width distribution) that allows (1.7) to be written in a single invariant form on each layer of the L_β hierarchy is directly related to the decay rate of TI across the L_β hierarchy. These facts underlie the $\propto \sqrt{\delta\nu/u_\tau}$ scaling of the widths of layers II and III (see Table 1.1). They are also physically relevant to the mean dynamics since, for example, the VF term in (1.7) is of leading order interior to layer IV in Fig. 1-1, i.e., up to $y^+ \simeq 2.6\sqrt{\delta^+}$. Recall that this location also has relevance to the distribution of turbulence kinetic energy since it nominally coincides with the outer spectral peak of Ψ_u, and simultaneously, where the correlation coefficient quantifying the inner/outer modulation effect crosses zero from positive to negative [Mathis et al. (2009a)]. These and other considerations discussed in section 1.3 motivate our use of the intermediate coordinate, $y/\sqrt{\nu\delta/u_\tau} = y^+/\sqrt{\delta^+}$, in this and subsequent sections. It is important, however, to keep in mind that the length scale, $\sqrt{\nu\delta/u_\tau}$, only reflects an average property of the underlying distribution of layer widths, $W(y^+)$.

Figures 3-2a-c display correlation coefficient maps from the laboratory data as a function of $-U\Delta t = \Delta x$, where U is the local mean velocity. All of the frames in this figure employ the same color scale, and, in each case, the vertical field of view extends from the closest measured position to $y^+ \simeq \delta^+$, while the horizontal scale spans $\Delta x^+ \simeq \pm\delta^+$. The horizontal line in each frame denotes the position $y^+ = 2.6\sqrt{\delta^+}$. The profiles of Fig. 3-1a are connected to those in Fig. 3-2 since at each δ^+ the $\Delta x^+ = 0$ correlation values comprise the corresponding inner-normalized profile in Fig. 3-1a.

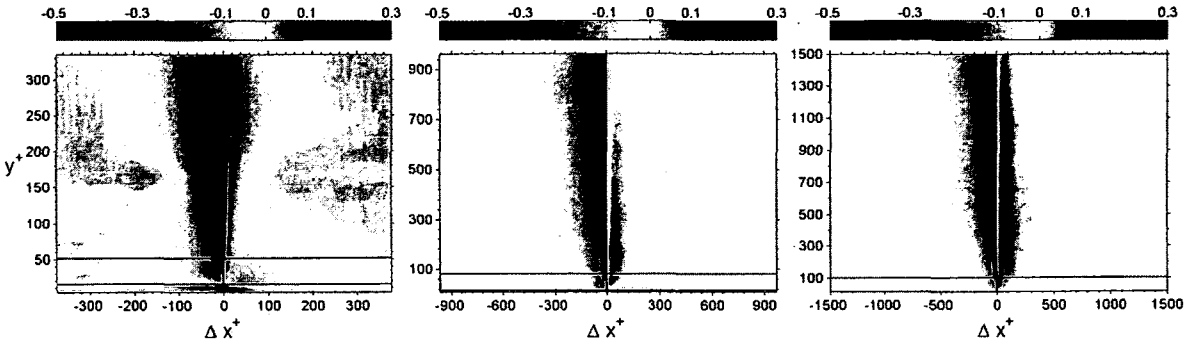

Figure 3-2. Color map of the correlation between $\omega_z(x^+)$ and $v(x^+ + \Delta x^+)$ as a function of y^+, (a) $\delta^+ = 375$, (b) $\delta^+ = 970$, (c) $\delta^+ = 1,500$. The streamwise separation, Δx^+, is estimated using Taylor's hypothesis and the local mean velocity.

Comparison of Figs. 3-2a-c reveals characteristic features, and clear Reynolds number dependencies. A primary observation is that, independent of Reynolds number and beginning interior to $y^+ = 2.6\sqrt{\delta^+}$, there emerges a region of significant negative correlation for $\Delta x^+ \leq 0$. The maximum amplitude of this negative correlation decreases with increasing δ^+, but its Δx^+ extent increases. By recognizing, however, that each frame spans $-\delta^+ \lesssim \Delta x^+ \lesssim \delta^+$, it becomes apparent that the outer-normalized streamwise extent of non-zero correlation in layer IV is a decreasing function of δ^+. (The scaling of these correlation lengths is explored further below.) There is also an emerging region of positive correlation at positive Δx^+ that increases in amplitude and outer-normalized wall-normal extent with increasing Reynolds number.

The results of Figs. 3-2a-c are similar to those recently presented for channel flow at $\delta^+ = 934$ [Monty et al. (2011)]/ The correlation maps in the boundary layer are not, however, expected to be exactly the same as in channels. To leading order, the pressure gradient in the channel balances the TI term in layer IV, while in the boundary layer TI is balanced by MI in layer IV. MI is a function of y^+ whose shape and amplitude change as δ^+ varies, while the pressure gradient in the channel only

depends on δ^+ [Klewicki et al. (2011)]. Features similar to those in the channel include the exclusively positive zone of correlation in the region $y^+ \lesssim 10$ (only accessible in the present $\delta^+ = 375$ results), and at the higher Reynolds numbers, the existence of the negative-to-positive zero-crossing along constant y^+ slices in layer IV. The fact that the long-time average is flanked between much larger positive and negative peaks (at $\pm\Delta x^+$ separations) is especially significant relative to the establishment of the mean momentum field, and the potential for its modification. As noted by Monty et al., [Monty et al. (2011)] this structure indicates that significantly different TI contributions to (1.7) would be realized through only small variations in the average phase relationship between the v and ω_z fluctuations.

This, and other related attributes, are exemplified by the individual Δx correlations in Figs. 3-3a-e. These figures show slices through the correlation maps of Figs. 3-2a-c at $y^+ \simeq 20$, $y/\sqrt{\nu\delta/u_\tau} \simeq 2.6$, and $y/\delta \simeq 0.3$ for each of the laboratory δ^+.

The profiles of Fig. 3-3a reveal that near the bottom of the layer hierarchy each of the correlations exhibit the same characteristic shape, but with increasing δ^+ the value of the correlation at $\Delta x^+ = 0$ shifts upward. It is also apparent that these correlations do not scale on Δx^+, as the individual peaks near $\Delta x^+ = 0$ do not align, and, with increasing δ^+, there is an increasingly longer tail of non-zero correlation for positive Δx^+. (Note that $R_{v\omega_z} \simeq 0$ for larger negative Δx^+ than shown.) Given the Reynolds number trend indicated by Figs. 3-2a-c, it is clear that the streamwise extent of the $R_{v\omega_z}$ correlation adheres to something intermediate to inner and outer scaling. This is made apparent by Fig. 3-3b, which shows that when Δx is normalized by $\sqrt{\nu\delta/u_\tau}$ the peaks at different δ^+ exhibit much closer alignment, and the tails of these correlations at positive Δx effectively merge. This remarkable finding is likely to be an important attribute of the inner/outer interaction discussed in the Introduction.

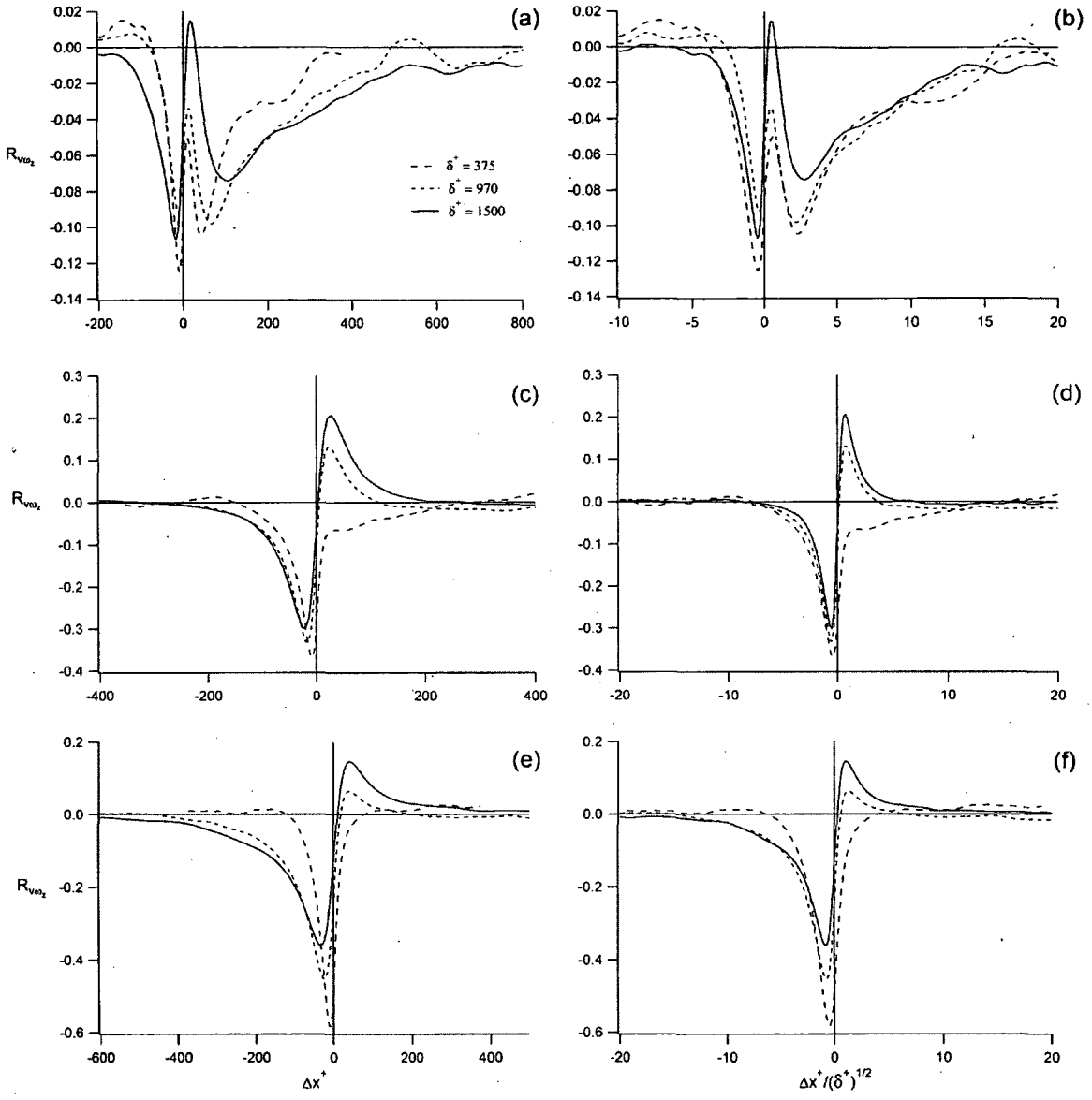

Figure 3-3. Correlation coefficient profiles of $\omega_z(x)$ and $v(x + \Delta x)$ at $y^+ \simeq 20$, $y/\sqrt{\nu\delta/u_\tau} \simeq 2.6$, and $y/\delta \simeq 0.3$; (a) $y^+ \simeq 20$: $R_{v\omega_z}$ versus Δx^+, (b) $y^+ \simeq 20$: $R_{v\omega_z}$ versus $\Delta x/\sqrt{\nu\delta/u_\tau}$, (c) $y/\sqrt{\nu\delta/u_\tau} \simeq 2.6$: $R_{v\omega_z}$ versus Δx^+, (d) $y/\sqrt{\nu\delta/u_\tau} \simeq 2.6$: $R_{v\omega_z}$ versus $\Delta x/\sqrt{\nu\delta/u_\tau}$, (e) $y/\delta \simeq 0.3$: $R_{v\omega_z}$ versus Δx^+, (f) $y/\delta \simeq 0.3$: $R_{v\omega_z}$ versus $\Delta x/\sqrt{\nu\delta/u_\tau}$. The streamwise separation, Δx, is estimated using Taylor's hypothesis and the local mean velocity.

The results for $y/\delta \simeq 0.3$ in Figs. 3-3e,f exemplify how the $R_{v\omega_z}$ correlation structure changes from layer II to layer IV, and thus also provides a useful context for interpreting the correlations near the outer edge of layer III shown in Figs. 3-3c,d. Unlike the near-wall correlations, those in Fig. 3-3e do not exhibit the strong negative excursion for positive Δx^+. Instead, they have a shape consistent with the passage of isolated spanwise vortices of either sign. Like the near-wall correlations, those at $y/\delta \simeq 0.3$ exhibit a consistent upward trend with increasing δ^+, and when plotted versus Δx^+ the correlation peaks clearly fail to align. Figure 3-3f shows that plotting versus $\Delta x/\sqrt{\nu\delta/u_\tau}$ causes the peaks to align even more convincingly than near $y^+ = 20$, and causes the $\pm\Delta x$ tails of the correlation to merge – especially at the two higher δ^+. The region of large correlation is significantly more compact at $y/\delta \simeq 0.3$, and an apparent Reynolds number dependence is exhibited by the emergence of an increasing positive peak for positive streamwise separation.

The correlations in Figs. 3-3c,d reveal that by the outer edge of layer III ($y^+ \simeq 2.6\sqrt{\delta^+}$) the large ($\Delta x^+ > 0$) negative peak seen in Fig. 3-3a is no longer present. Inspection of the correlations between $y^+ \simeq 20$ and $y^+/\sqrt{\delta^+} = 2.6$ (not shown) reveals that, for positive Δx^+ the upward peak (positive at $\delta^+ = 1500$) in Fig. 3-3a continues to move upward, while the negative peak moves toward zero and shifts to increasing Δx^+ until it effectively becomes the *knee* in the downward portion of the positive peak at positive Δx^+ shown in Fig. 3-3c. The $\delta^+ = 375$ profile, which never develops a positive peak for $\Delta x^+ > 0$, still shows a hint of the negative peak in Fig. 3-3c. This negative peak is no longer prominent in the profiles by about $y^+ = 40$. Note, however, that at $\delta^+ = 375$ $y^+ = 2.6\sqrt{\delta^+} \simeq 50$, and thus unlike the higher δ^+, at this Reynolds number the mean dynamics become inertially dominated very close to where where this near-wall feature diminishes. As with the correlation of Figs. 3-

3b and f, normalization of Δx by $\sqrt{\nu\delta/u_\tau}$ results in a convincing alignment of the correlation peaks.

The scaling behaviors of the correlations in Figs. 3-2a-c are quantitatively explored by estimating a length scale that characterizes the extent of non-zero correlation. Following Monty et al, [Monty et al. (2011)] this characteristic length scale is (subjectively) defined as the streamwise distance over which the correlation profile at each fixed y^+ (e.g., as in Figs. 3-3) exceeds 30% of its maximum amplitude. The results from the data underlying the correlation maps of Figs. 3-2 are shown in Figs. 3-4a-d. Calculation of these correlation lengths required long time series. These were available from the laboratory data, albeit even the laboratory $u\omega_z$ correlation lengths exhibit considerable scatter, see Figs. 3-7a,b below. The signal length requirement, however, prevented reliable estimates from the field data.

The results of Fig. 3-4a show the inner-normalized $v\omega_z$ streamwise correlation lengths, $l_x^+(v\omega_z)$, as a function of y^+. Notable profile features include a highly localized near-wall maximum that decreases to a minimum with increasing y^+, and beyond which they exhibit a continuous increase out to $y^+ = \delta^+$. Under this normalization, the amplitude of the near-wall maximum is a strongly increasing function of δ^+, but its position appears to be essentially fixed. Beyond the minimum, the laboratory profiles of Fig. 3-4a exhibit a weak increase in magnitude with increasing Reynolds number, with the two higher δ^+ profiles showing good agreement. As with a number of statistics, the differences exhibited by the $\delta^+ = 375$ data are likely to be a result of its being at a Reynolds number that is only just barely within the four layer regime.

Fig. 3-4b provides evidence that when $l_x(v\omega_z)$ is normalized by $\sqrt{\nu\delta/u_\tau}$ and plotted versus y^+ the Reynolds number dependence of the near-wall peak is effectively removed. Under this normalization, however, the portion of the profiles beyond their minimums exhibit a clear decreasing trend with δ^+. In this region, the profiles at

$\delta^+ = 970$ and 1500 are nearly parallel, and over a portion of this outer domain appear to exhibit an approximately logarithmic variation. The region bounding the near-wall peak in Figs. 3-4a,b (between the vertical dashed lines) begins near the lower boundary of the L_β hierarchy and extends to $y^+ \simeq 40$. Previous analysis of the velocity gradients contributing to the spanwise vorticity fluctuations reveal that the correlation coefficient, $R_{\frac{\partial u}{\partial y}\frac{\partial v}{\partial x}}$, exhibits a positive peak in this region, but is negative everywhere else in the boundary layer. A positive value for this correlation indicates motions of high strainrate, as opposed to motions more akin to solid-body rotation [Klewicki & Falco (1996)]. In addition, recent analysis of the spatial fluxes in turbulent channel flow provide evidence indicating that over the region, $6 < y^+ < 37$, there is an inverse cascade in which energy is transferred from the small to larger scales [Saikrishnan et al. (2012)]. These findings and observations, along with the results in section 3.2.2, collectively identify the peak region in Figs. 3-4a,b as one of intense vortex stretching. The near-wall magnitude of l_x scales with $\sqrt{\nu\delta/u_\tau}$, and this leads one to suspect that the large scale modulation of the near-wall flow may in fact dictate the initial scale at which the near-wall vorticity field three-dimensionalizes.

From the theory described in the Introduction, normalizing l_x and y by $\sqrt{\nu\delta/u_\tau}$ is expected to cause the profiles to merge (with increasing accuracy as $\delta^+ \to \infty$) over a region starting near the outer edge of layer III, and ending near the upper end of the hierarchy, $y/\delta \simeq 0.5$. This normalization is shown in Fig. 3-4c. The profiles from the two higher Reynolds number profiles demonstrate the expected behavior, exhibiting very good agreement starting near $y/\sqrt{\nu\delta/u_\tau} = 2.6$, and diverging in the region beyond $y/\delta = 0.5$. The $\delta^+ = 375$ data appear to merge with the other profiles for a small domain beyond the outer edge of layer III, and then clearly diverge near $y/\delta = 0.5 \simeq y/\sqrt{\nu\delta/u_\tau} = 10$. The fact that the $\delta^+ = 375$ data merges with the others at a point slightly beyond $y^+/\delta^+ = 2.6$ is consistent with the lack of any appreciable

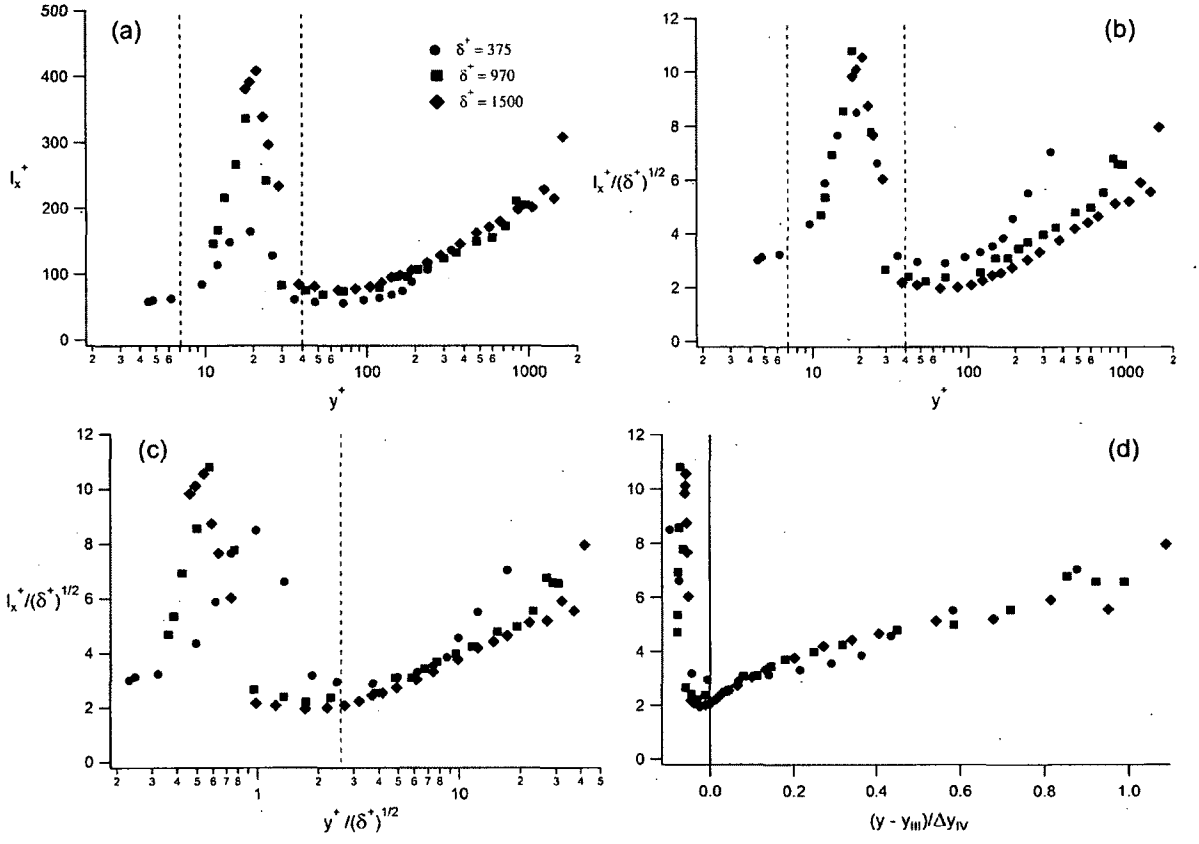

Figure 3-4. Profiles of the characteristic streamwise lengths associated with the $v\omega_z$ correlations of Fig. 3-2. (a) l_x^+ versus y^+, (b) $l_x^+/\sqrt{\delta^+}$ versus y^+, (c) $l_x^+/\sqrt{\delta^+}$ versus $y^+\sqrt{\delta^+}$, (d) $l_x^+/\sqrt{\delta^+}$ versus $(y^+ - 2.6\sqrt{\delta^+})/(\delta^+ - 2.6\sqrt{\delta^+})$.

scale separation at this Reynolds number. The wavelength data of Fig. 3-16 below exhibit similar behavior.

The representation of Fig. 3-4c seeks to scale the streamwise correlation lengths of $R_{v\omega_z}$ by aligning the data at the outer edge of layer III (i.e., where the VF term in (1.7) loses leading order status), and using geometric mean of the $W(y^+)$ distribution as the characteristic length. According the theory, this *inside-out* scaling should only hold out to the upper limit of the hierarchy. Alternatively, the theory also suggests an *outside-in* scaling based upon the width of layer IV. This involves plotting $l_x/\sqrt{\nu\delta/u_\tau}$ versus $(y^+ - 2.6\sqrt{\delta^+})/(\delta^+ - 2.6\sqrt{\delta^+})$, which shifts the origin to the outer edge of layer III, and normalizes the remaining distance by the thickness of layer IV. Note that as $\delta^+ \to \infty$, this normalization becomes essentially equivalent to plotting the data versus y/δ, see Table 1.1. At the low Reynolds numbers of the present study, however, use of y/δ noticeably shifts the profiles out of alignment. Fig. 3-4d presents the present data under this normalization. Close examination of the $\delta^+ = 970$ and $1,500$ data reveals this to be the most convincing normalization for layer IV, while the scatter of the lowest Reynolds number data reveals no consistent trend. Presenting the data under this normalization also provides a clearer indication of the abrupt change that occurs in this statistic near the position where the VF term in (1.7) loses leading order. In the context of the present theory, the origin of the horizontal axis of Fig. 3-4d precisely marks the onset of the "outer" or inertial scaling domain.

The correlation maps of $\omega_z(x^+)$ and $u(x^+ + \Delta x^+)$ are shown for $y^+ \leq 100$ and $y^+ \geq 50$ in Figs. 3-5a-c and d-f, respectively. Owing to their variation with distance from the wall and Reynolds number, each frame is assigned a separate color scale. The horizontal white lines identify $y^+ = 15$ and $y/\sqrt{\nu\delta/u_\tau} = 2.6$. These bounds are very close the full wall-normal range of Fig. 3-5c which extends from $y^+ \geq 17$ to $y/\sqrt{\nu\delta/u_\tau} \leq 2.58$. The streamwise extent of each frame is $-\delta^+ \lesssim \Delta x^+ \lesssim \delta^+$.

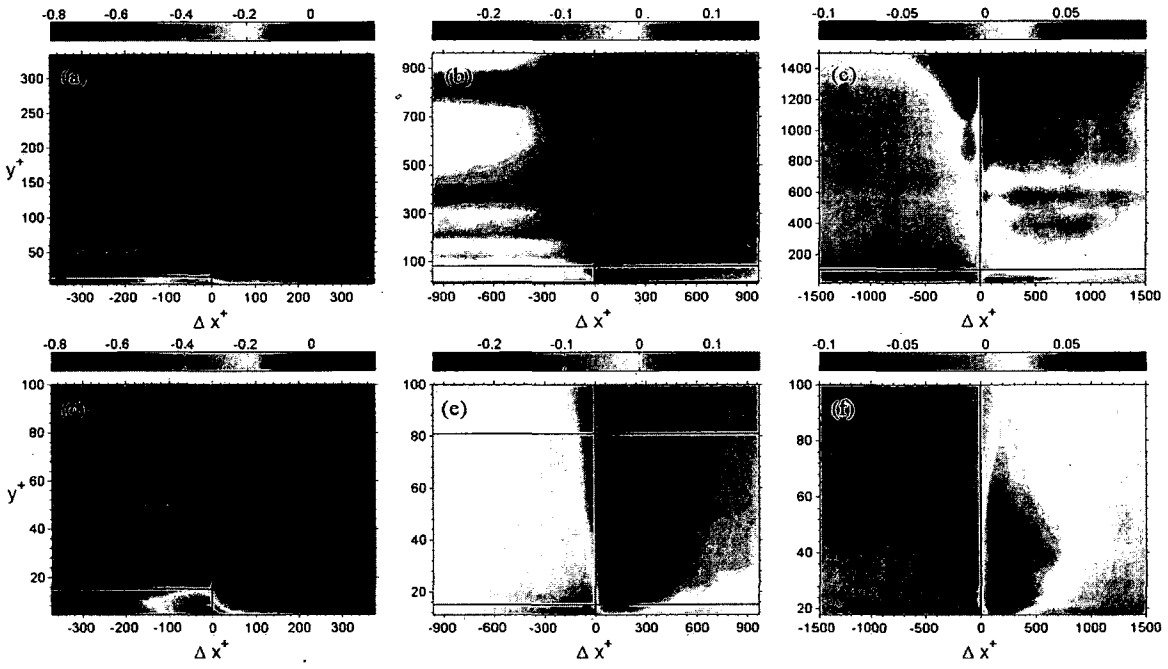

Figure 3-5. Color map of the correlation between $\omega_z(x^+)$ and $u(x^+ + \Delta x^+)$ as a function of y^+, Row 1: $y^+ \leq 100$, (a) $\delta^+ = 375$, (b) $\delta^+ = 970$, (c) $\delta^+ = 1,500$. Row 2: $y^+ \geq 50$, (d) $\delta^+ = 375$, (e) $\delta^+ = 970$, (f) $\delta^+ = 1,500$. The streamwise separation, Δx^+, is estimated using Taylor's hypothesis and the local mean velocity. The horizontal lines denote $y^+ = 15$ and $y/\sqrt{\nu\delta/u_\tau} = 2.6$.

Visual inspection of Figs. 3-5a-c leads one to suspect that, like the $R_{v\omega_z}$ contours, the outer-normalized extent of the $R_{u\omega_z}$ correlation is a decreasing function of Reynolds number. As shown below, however, this turns out not to be the case owing to the apparent combined influence of two characteristic scales. A distinctive trait held by all of the near-wall correlations is the alignment of the negative-to-positive zero-crossing of the correlation contours with the position of maximum u'^+ near $y^+ = 15$. This stems from (1.5), and the fact that that $\overline{u^2}^+$ is the dominant contributor to q^+. Similarly, (1.5) indicates that the positive values of $R_{u\omega_z}$ along $\Delta x^+ = 0$ for $y^+ > 15$ are in accord with a decreasing $q^+(y^+)$ function, i.e., $\partial q^+/\partial y^+ < 0$. For greater wall-normal positions, the positive amplitude of $R_{u\omega_z}$ diminishes along $\Delta x^+ = 0$, and especially so with increasing Reynolds number. This reflects the emergence of the u'^+ plateau region with increasing δ^+. In this region $R_{u\omega_z}$ is negative for $\Delta x^+ < 0$, positive for $\Delta x^+ > 0$, and this demarcation becomes more distinct with increasing Reynolds number. Collectively, both the inner and outer frames of Fig. 3-5 indicate that the position of minimally positive $R_{u\omega_z}$ is located near the outer edge of layer III.

The outer contours of Figs. 3-5d-f exhibit features that are subtle and complex. At $\delta^+ = 375$, the zone of positive correlation centered about $\Delta x^+ = 0$ is flanked by regions of essentially zero correlation. The $\Delta x^+ < 0$ region of zero correlation is significantly more narrow than the one located at $\Delta x^+ > 0$. For larger negative Δx^+ there exists a significant region of mildly negative correlation. With increasing δ^+, the flanking zones of zero correlation diminish, and there emerges a more well-defined structure of negative correlation for $\Delta x^+ < 0$ and positive correlation for $\Delta x^+ > 0$. As $y^+ \to \delta^+$ the values of $R_{u\omega_z}$ in the vicinity of $\Delta x^+ = 0$ become increasingly positive. This is consistent with the rapid decrease in $q^+(y^+)$ as the freestream is approached.

The outer region correlation maps at the two higher δ^+ provide evidence of a cell-like structure that withstands time averaging.

Similar to Figs. 3-3a-f, the rows of Fig. 3-6 display the individual $R_{u\omega_z}(\Delta x)$ profiles at $y^+ \simeq 20$, $y/\sqrt{\nu\delta/u_\tau} \simeq 2.6$, and $y/\delta \simeq 0.3$. The correlations plotted versus Δx^+ (not shown) reveal that both the peaks near $\Delta x = 0$ and the tails of the correlations are predominantly characterized by scales larger than the viscous length. Figures 3-6a-f respectively plot $R_{u\omega_z}$ versus $\Delta x/\sqrt{\nu\delta/u_\tau}$ and $\Delta x/\delta$ at each wall-normal location.

The correlations of Figs. 3-6a,b are characterized by an abrupt zero-crossing near $\Delta x = 0$. In this regard, note that the value of $R_{u\omega_z}$ at $\Delta x = 0$ is very close to zero as $y^+ = 20$ is just beyond the near-wall peak in q^+. The $\delta^+ = 375$ profile exhibits the largest negative peak, and the $\delta^+ = 970$ profile contains the largest positive peak. The $\delta^+ = 970$ and $1,500$ profiles exhibit much closer agreement, with their negative peaks showing nearly identical shape and amplitude, and their positive peaks showing similar shape but slightly different amplitude. The positive and negative peaks in these profiles exhibit good alignment under the normalization of Fig. 3-6a, but, as quantified in Fig. 3-7b below, the overall characteristic length of $R_{u\omega_z}$ in this part of the flow appears to best scale with δ. While the relatively slowly varying behavior of the u'^+ profile tends to support the view that near-wall structure is largely an autonomous function of inner scaling, the results of Figs. 3-6a,b reveal that the near-wall correlations contributing to $\partial q^+/\partial y^+$ undergo significant changes with δ^+.

The $\delta^+ = 375$ profile at $y/\sqrt{\nu\delta/u_\tau} \simeq 2.6$ in Fig. 3-6c exhibits a dramatic variation from its shape at $y^+ \simeq 20$. At this location the large negative peak at slightly negative Δx has now disappeared, and the correlation profile is characterized by a single dominant positive peak at slightly positive Δx. On the other hand, the two higher δ^+ profiles continue to have qualitative similarities with those at $y^+ = 20$. One

noticeable difference is that for $\Delta x/\sqrt{\nu\delta/u_\tau} < 0$ the two lower δ^+ profiles now show close agreement, with the $\delta^+ = 1,500$ correlation exhibiting a similar shape but larger negative values for $\Delta x/\sqrt{\nu\delta/u_\tau} < 0$. The profile peaks at negative Δx exhibit good alignment under the normalization of Fig. 3-6c. For positive Δx, however, the positive peaks do not align when Δx is normalized by $\sqrt{\nu\delta/u_\tau}$, and even the normalization by δ in Fig. 3-6d is not sufficient to cause these peaks to align. The correlation structure for negative Δx in this figure appears to scale reasonably with δ, but for positive Δx the low Reynolds number profile rapidly crosses over to negative values, while the two higher δ^+ profiles exhibit a more gradual decrease to zero. Overall, the structure emerging with increasing δ^+ is characterized by a significant zone of negative correlation for $\Delta x/\delta < 0$, an abrupt transition through zero near $\Delta x/\delta = 0$, followed by an extended zone of positive correlation for $\Delta x/\delta < 0$, also see Figs. 3-5.

The results at $y/\delta \simeq 0.3$ are shown in Figs. 3-6e,f. Outward from layer III the negative ($\Delta x < 0$) peak in $R_{u\omega_z}$ seems to reasonably adhere to outer scaling, while the positive ($\Delta x > 0$) peak moves to increasing $\Delta x/\delta$ with increasing δ. Overall, this seems to indicate that, at least at these low Reynolds numbers, there are important physics that increase in size at a faster rate than does the largest characteristic length scale. As with the results at $y^+/\sqrt{\delta^+} \simeq 2.6$, the $\delta^+ = 375$ correlation exhibits a distinctly different shape, and this is consistent with the rapid evolution of the outer region flow at low Reynolds numbers. Close examination of the $\delta^+ = 1,500$ profile of Fig. 3-6e shows an interesting *jog* in the profile near $\Delta x = 0$, and subtle evidence of this is also observed in the $\delta^+ = 1,500$ profile of Fig. 3-6c. This may reflect the emergence of an internal structure to these correlations with increasing δ^+.

Characteristic lengths associated with the $R_{u\omega_z}$ correlations of Figs. 3-5 are shown in Figs. 3-7a,b. From these it is apparent that the $l_x(u\omega_z)$ profiles exhibit significantly more scatter than do those for $l_x(v\omega_z)$ in Fig. 3-4. This results from the fact that

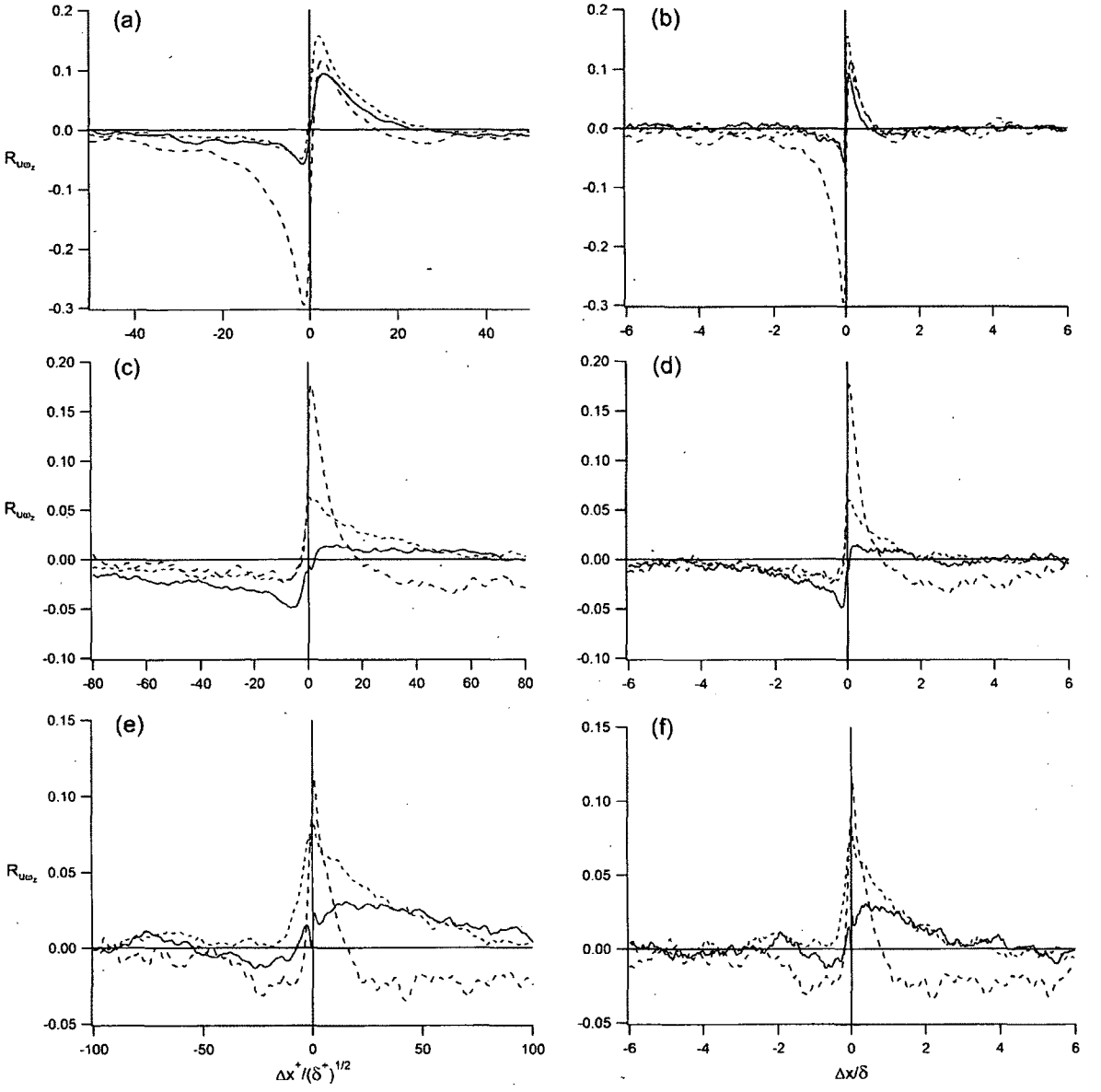

Figure 3-6. Correlation coefficient profiles of $\omega_z(x)$ and $u(x+\Delta x)$ at $y^+ \simeq 20$, $y/\sqrt{\nu\delta/u_\tau} \simeq 2.6$, and $y/\delta \simeq 0.3$; (a) $y^+ \simeq 20$: $R_{u\omega_z}$ versus $\Delta x/\sqrt{\nu\delta/u_\tau}$, (b) $y^+ \simeq 20$: $R_{u\omega_z}$ versus $\Delta x/\delta$, (c) $y/\sqrt{\nu\delta/u_\tau} \simeq 2.6$: $R_{u\omega_z}$ versus $\Delta x/\sqrt{\nu\delta/u_\tau}$, (d) $y/\sqrt{\nu\delta/u_\tau} \simeq 2.6$: $R_{v\omega_z}$ versus $\Delta x/\delta$, (e) $y/\delta \simeq 0.3$: $R_{u\omega_z}$ versus $\Delta x/\sqrt{\nu\delta/u_\tau}$, (f) $y/\delta \simeq 0.3$: $R_{u\omega_z}$ versus $\Delta x/\delta$. The streamwise separation, Δx^+, is estimated using Taylor's hypothesis and the local mean velocity.

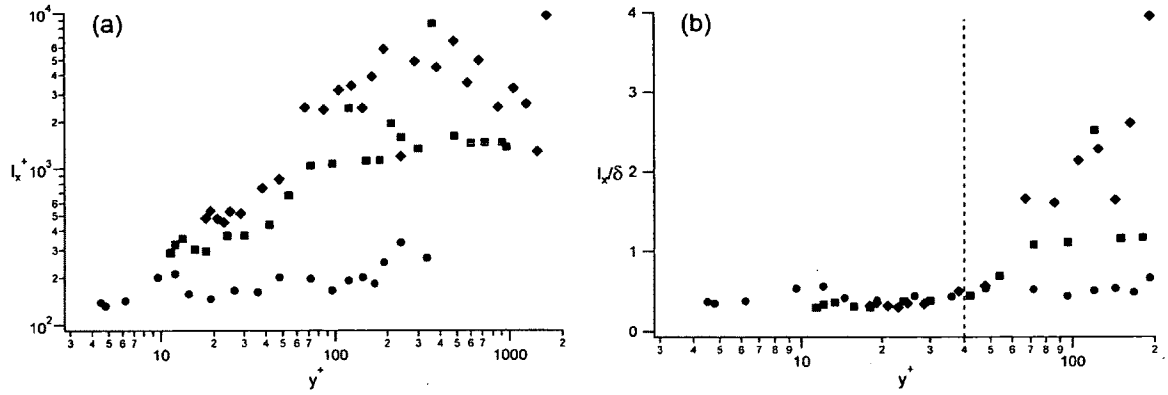

Figure 3-7. Profiles of the characteristic streamwise lengths associated with the $u\omega_z$ correlations of Fig. 3-5. (a) l_x^+ versus y^+, (b) l_x/δ versus y^+.

these correlations extend over a much larger streamwise distances. Even with this additional uncertainty, it is clear from the l_x^+ versus y^+ profiles of Fig. 3-7a that the correlation lengths undergo dramatic variations over the given δ^+ range. Near the wall, the trends in these profiles suggest that they may merge to follow inner scaling in the region interior to the peak in u'^+. Outward from $y^+ \simeq 17$, however, the data follow increasingly steeper upward trends with increasing δ^+, and give some indication that upon passing into layer IV (beyond $y^+/\sqrt{\delta^+} \simeq 2.6$) they level-off. The profiles of Fig. 3-7b show the notable result that from $y^+ \simeq 15$ to $y^+ \simeq 40$ the $R_{u\omega_z}$ correlation lengths merge onto a single profile when normalized by the outer length scale, δ, and plotted versus y^+. This provides a rather unambiguous indication that outer region motions influence the behavior of the near-wall turbulence kinetic energy gradient by dictating the length scales of the relevant interactions. It is also clear from Fig. 3-7b that beyond $y^+ \simeq 40$ the profile increase at distinctly different rates, and that these rates out-pace the growth of δ.

3.2 Spectral Behaviors

Estimates of the u, v and ω_z spectra were determined using the methods described in section 2.2. In this section these spectra are analyzed to investigate the scale selection and scale separation phenomena discussed in section 1.4.

3.2.1 Scale Selection

Scale selection is investigated by documenting the behaviors of the velocity vorticity cospectra relative to their contributing velocity and vorticity spectra, and as a function of Reynolds number and distance from the wall. The spectra herein are plotted versus streamwise wavelength and are presented in pre-multipled form. The cospectrum is normalized such that its integral is the correlation coefficient. The peaks in the individual velocity and vorticity spectra move apart with increasing Reynolds number, and as a result, detection of whether the associated cospectrum is tracking one or the other spectra is most easily detected under the condition of appreciable scale separation. For this reason, variations with wall-normal position are documented at the highest laboratory Reynolds number, $\delta^+ = 1,500$, and Reynolds number variations are investigated by comparing these with the field results at $\delta^+ \simeq 8.9 \times 10^5$.

Figures 3-8a-d show the spectra of v and ω_z and their cospectra at $y^+ = 24.8$, $y/\sqrt{\nu\delta/u_\tau} = 1.23$, $y/\sqrt{\nu\delta/u_\tau} = 3.21$, and $y/\delta = 0.83$, respectively. At the near-wall position, the cospectrum exhibits at characteristic shape that features a positive peak at small wavelengths and a negative peak at larger wavelengths. At this position, the v and ω_z spectra are nearly identical, and thus one is unable to surmise whether either of the cospectral peaks can be attributed primarily to v or ω_z. With increasing distance from the wall, however, the characteristic wavelengths v and ω_z separate. By $y/\delta = 0.83$ (Fig. 3-8d), the peak in Ψ_v^+ is at a wavelength that is about 5 times larger than the peak in $\Psi_{\omega_z}^+$. As evidenced by the relatively invariant position of the ω_z

spectrum, this separation primarily occurs owing to the v spectrum shifting to larger scales. By $y/\sqrt{\nu\delta/u_\tau} = 1.23$ ($y^+ = 47.6$, at this δ^+) there is no longer a positive peak in the cospectrum, and the negative peak has attenuated. From the totality the laboratory data, it is observed that across layer III ($1.6 \lesssim y/\sqrt{\nu\delta/u_\tau} \lesssim 2.6$) the positive peak never re-emerges, and the negative peak further attenuates. Into layer IV, however, a distinctive negative peak becomes apparent. As shown in Fig. 3-8c, the cospectrum at $y/\sqrt{\nu\delta/u_\tau} = 3.21$ is a nearly perfect mirror image of the v spectrum, indicating that the contributions to the TI term in (1.7) from $\overline{v\omega}$ apparently arise owing to a scale selection with the v velocity. This v dominated scale selection persists to positions near the outer edge of the boundary layer, Fig. 3-8d.

Figures 3-9a,b respectively show the v and ω_z spectra and cospectra near $y/\sqrt{\nu\delta/u_\tau} = 1.36$ and 4.08 at $\delta^+ \simeq 8.9 \times 10^5$. The data of Fig. 3-9a reveal that there is considerable scale separation by $y/\sqrt{\nu\delta/u_\tau} = 1.36$, and that the small positive peak in the cospectrum results from a scale selection with the peak in $\Psi^+_{\omega_z}$. Similar to the $\delta^+ = 1,500$ results, there exists a low level negative portion to the cospectrum at this location. At $y/\sqrt{\nu\delta/u_\tau} = 4.08$, the scale separation between the peaks in the v and ω_z spectra is about 1.5 decades in wavelength, and the positive peak at small wavelengths is essentially non-existent. Similar to the low δ^+ results, the onset of layer IV is accompanied by a clear scale selection between the cospectrum and the spectrum of v.

The spectra and cospectra affiliated with u and ω_z at $\delta^+ = 1,500$ are shown in Figs. 3-10a-d. Distinct from the Ψ^+_v, the peak in Ψ^+_u exhibits about 1/2 decade of scale separation from the peak in $\Psi^+_{\omega_z}$ at $y^+ = 24.8$ (Fig. 3-10a). At this position, the cospectrum displays two distinctive peaks (negative at small wavelengths and positive at large wavelengths), suggesting simultaneous scale selections affiliated with $\Psi^+_{\omega_z}$ and Ψ^+_u – albeit the alignment of the spectral and cospectral peaks is not perfect. Note

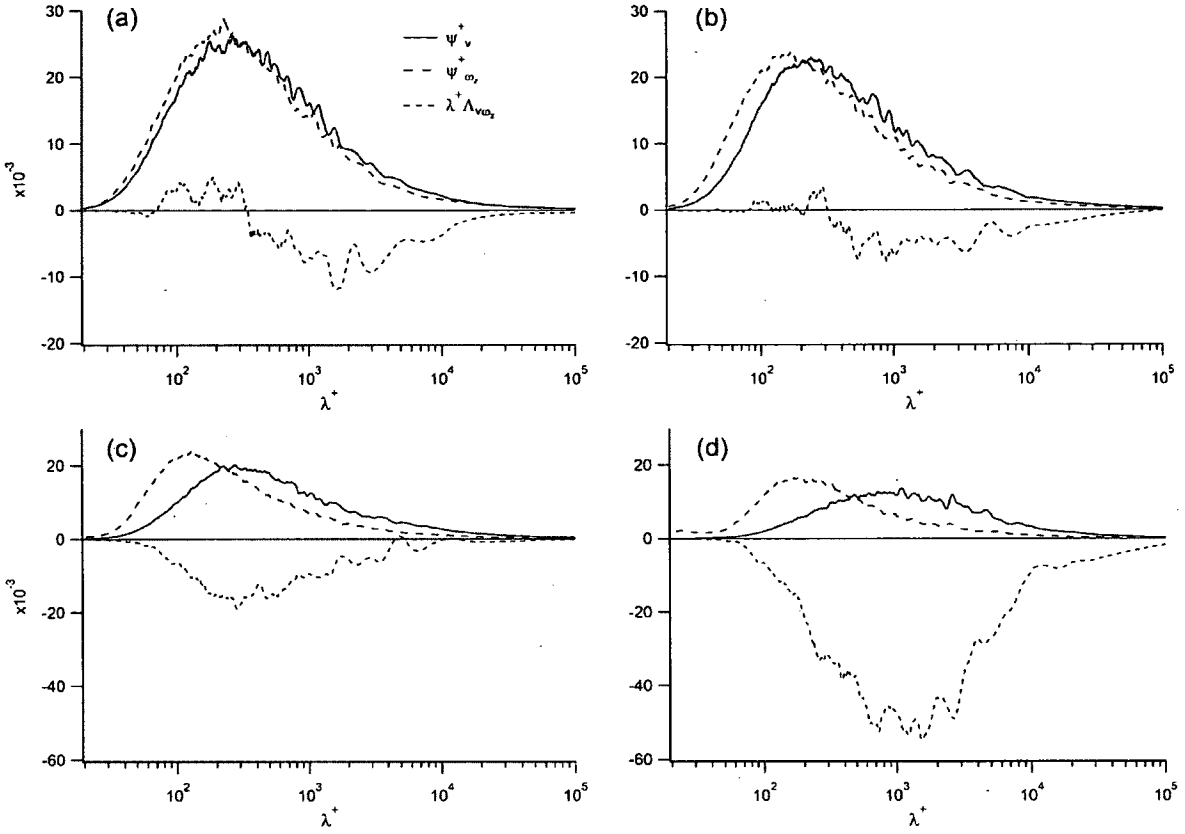

Figure 3-8. Pre-multiplied spectra of v and ω_z and their cospectra versus inner normalized wavelength at $\delta^+ = 1,500$, (a) $y^+ = 24.8$, (b) $y/\sqrt{\nu\delta/u_\tau} = 1.23$, (c) $y/\sqrt{\nu\delta/u_\tau} = 3.21$, (d) $y/\delta = 0.83$.

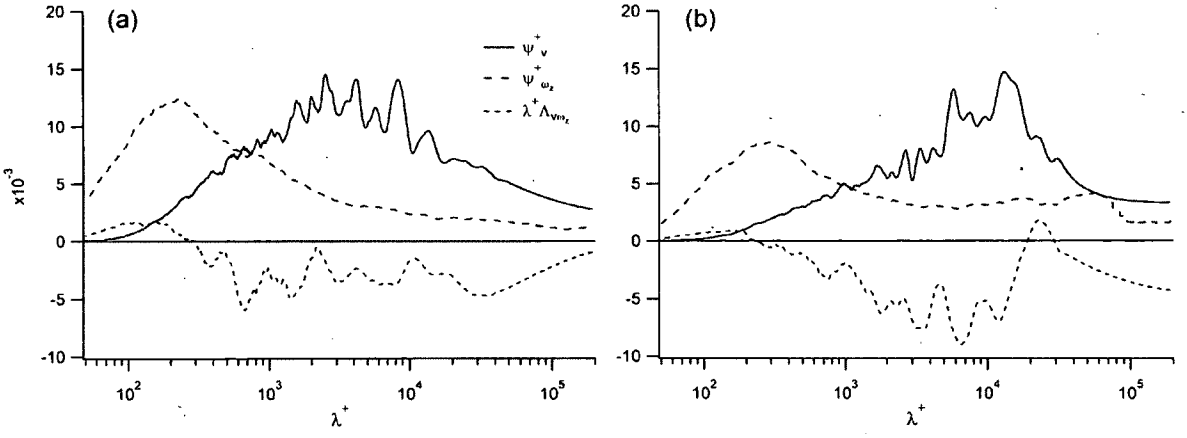

Figure 3-9. Pre-multiplied spectra of v and ω_z and their cospectra versus inner normalized wavelength at $\delta^+ \simeq 8.9 \times 10^5$, (a) $y/\sqrt{\nu\delta/u_\tau} = 1.36$, (b) $y/\sqrt{\nu\delta/u_\tau} = 4.08$.

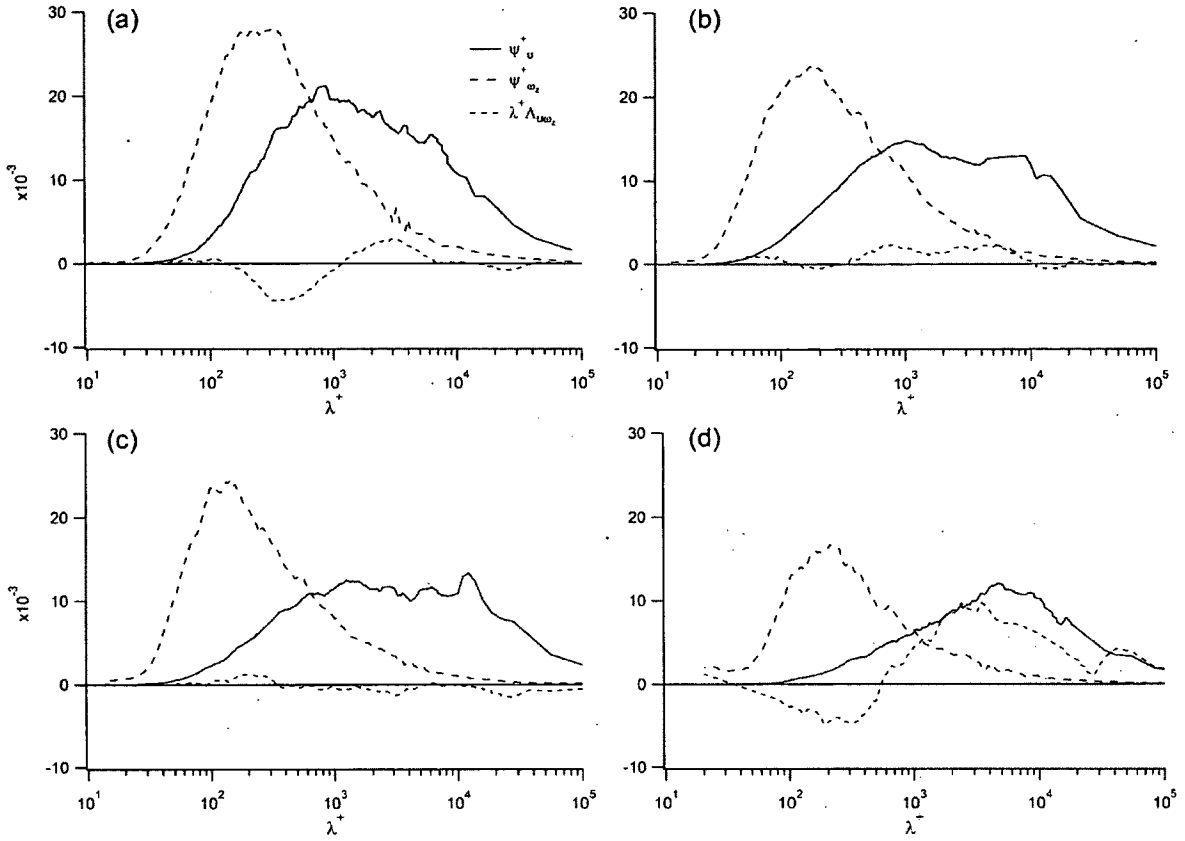

Figure 3-10. Pre-multiplied spectra of u and ω_z and their cospectra versus inner normalized wavelength at $\delta^+ = 1,500$, (a) $y^+ = 24.8$, (b) $y/\sqrt{\nu\delta/u_\tau} = 1.23$, (c) $y/\sqrt{\nu\delta/u_\tau} = 3.21$, (d) $y/\delta = 0.83$.

that at $y^+ = 24.8$, $\partial q^+/\partial y^+$ is strongly negative. Consistent with the plateau region in q^+, the cospectra in Figs. 3-10b,c (at positions bounding layer III) exhibit nearly zero values. From near the wall to a position just outside of layer III, the weight in the u spectrum continually shifts to larger wavelengths, exhibiting something close to a horizontal plateau in Fig. 3-10c. In the outer part of the layer, where $\partial q^+/\partial y^+$ becomes strongly negative again, clear scale selections are re-established.

The u and ω_z spectra and cospectra at $\delta^+ \simeq 8.9 \times 10^5$ are shown in Figs. 3-11a,b. At $y/\sqrt{\nu\delta/u_\tau} = 0.64$ the wavelengths corresponding to the peaks in the u and ω_z spectra are different by a factor greater than $1,000$. Like the lower Reynolds number

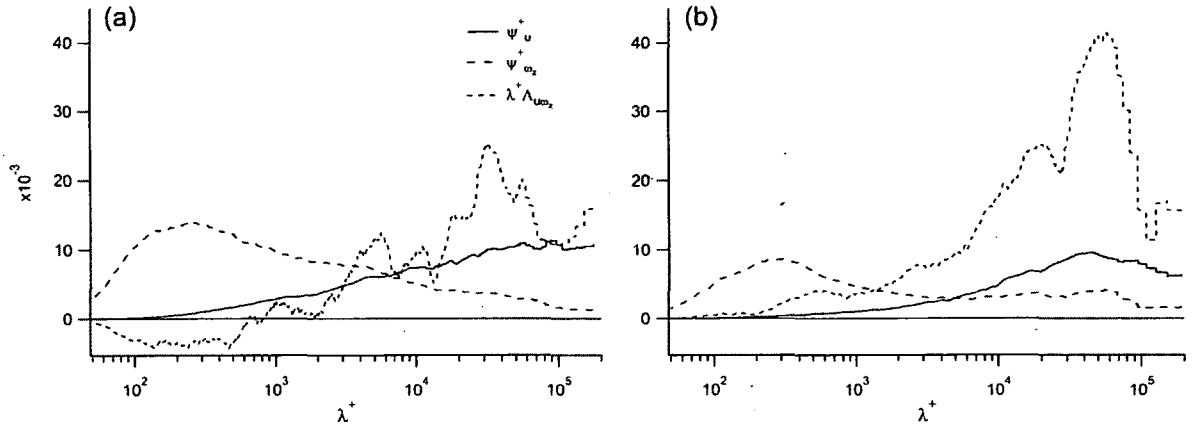

Figure 3-11. Pre-multiplied spectra of u and ω_z and their cospectra versus inner normalized wavelength at $\delta^+ \simeq 8.9 \times 10^5$, (a) $y/\sqrt{\nu\delta/u_\tau} = 0.64$, (b) $y/\sqrt{\nu\delta/u_\tau} = 4.08$.

cospectrum in the lower part of layer II, that in Fig. 3-11a exhibits a negative scale selection with the peak in $\Psi^+_{\omega_z}$ at small wavelength, and a positive peak that occurs near to, but less than, the peak in Ψ^+_u. These peaks appear to be separated by about three decades in wavelength. It is evident, however, that the u spectrum is truncated, and thus these data have poor spectral resolution at large wavelengths. Into layer IV ($y/\sqrt{\nu\delta/u_\tau} = 4.08$, Fig. 3-11b), the cospectrum exhibits a single positive peak, and an overall shape indicating a strong correspondence with Ψ^+_u. The results of Figs. 3-11a,b suggest that the scale separation between $\Psi^+_{\omega_z}$ and Ψ^+_u gets slightly smaller in moving from $y/\sqrt{\nu\delta/u_\tau} = 0.64$ to $y/\sqrt{\nu\delta/u_\tau} = 4.08$. As shown below, however, there is considerable scatter in the measured positions of the peaks of the u spectra, and thus the example results of Figs. 3-11a,b should be taken to be more qualitative than quantitative.

3.2.2 Scale Separation

Consistent with the depiction of Fig. 1-4, the figures of section 3.2.1 above indicate that the separation between the peaks in the streamwise wavelength spectra of velocity

and vorticity depends on Reynolds number and distance from the wall. This section further explores these behaviors by measuring the peak wavelengths of Ψ_u, Ψ_v and Ψ_{ω_z} (denoted λ_u, λ_v, and λ_{ω_z}, respectively), and by subsequently quantifying the net scale separation via the ratio of these wavelengths.

Figure 3-12 plots the inner-normalized streamwise wavelengths corresponding to the peak values of Ψ_u as a function of wall-normal distance and δ^+. The $\delta^+ = 375$ data in Fig. 3-12a indicate that at $y^+ = 5$ $\lambda_u^+ \simeq 300$. The λ_u^+ values increase with increasing y^+. The data suggest that across a near-wall region the profiles at different δ^+ merge when plotted versus y^+, and with increasing δ^+ they peel-off and plateau at increasingly larger values. The $\delta^+ = 970$ and $1,500$ profiles exhibit features that are alike, and together are somewhat different from the profile at $\delta^+ = 375$, which is only at the onset of the four layer regime. The $\delta^+ \simeq 8.9 \times 10^5$ data are at considerably higher magnitude, and exhibit a large scatter. As discussed relative to the spectra shown in section 3.2.1, this scatter arises owing the small ensemble size and poor spectral resolution at the large wavelengths characteristic of the peaks in Ψ_u. Overall, the much larger values and apparent increasing trend are qualitatively consistent with the profile behaviors at smaller δ^+.

The position at which the profiles level-off in Fig. 3-12a exhibits an apparent δ^+ dependence. To explore this, the data are re-plotted versus $y^+/\sqrt{\delta^+}$ in Fig. 3-12b. Under this normalization the low δ^+ profiles nominally level-off at $y^+/\sqrt{\delta^+} \simeq 3$, which is close to the outer edge of layer III in Fig. 1-1. It is also evident that the profiles remain distinct near the wall, while in Fig. 3-12a they apparently merge near the wall. The cluster of data at $\delta^+ \simeq 8.9 \times 10^5$ is, once again, qualitatively consistent with the low δ^+ trends, but given their scatter not much more can be reliably concluded. Under this normalization it is clear, however, that only a small fraction of these data exceed the $y^+/\sqrt{\delta^+} \simeq 3$ position where the low δ^+ data level-off.

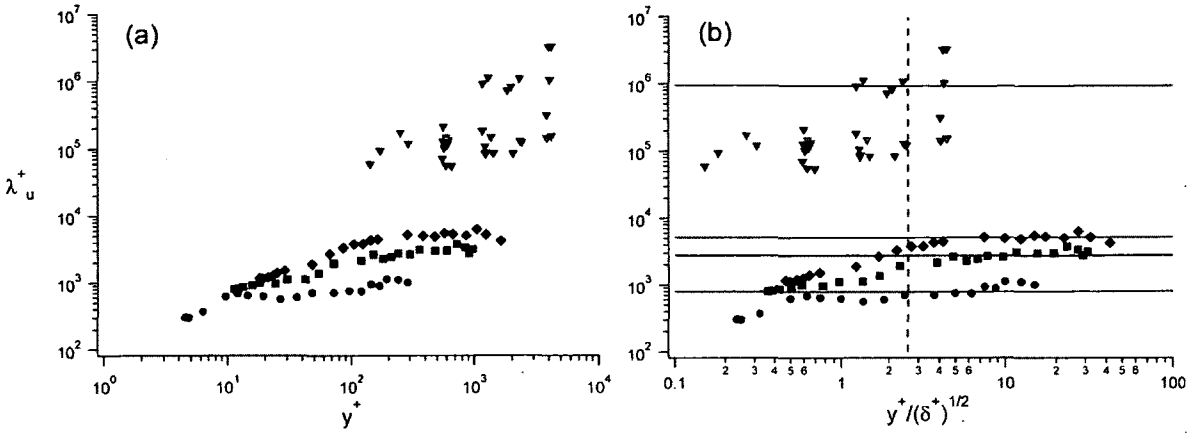

Figure 3-12. Wall-normal profiles of the inner-normalized wavelengths at which Ψ_u peaks; (a) versus y^+, (b) versus $y^+/\sqrt{\delta^+}$. Symbols same as in Fig. 2-1.

The inner-normalized wavelengths of Figs. 3-12a,b increase with increasing δ^+. To explore this further, Fig. 3-13 plots the plateau values of λ_u/δ versus δ^+. The plateau values are indicated by the horizontal lines on Fig. 3-12b. The high δ^+ value is estimated from the average of the ensemble of measurements for which $y/\sqrt{\delta^+} > 2$ in Fig. 3-12b. The error bar on the present high Reynolds number data point represents the full data scatter of this ensemble. Fig. 3-13 also plots the values of λ_u/δ^+ at the position of the outer spectral peak estimated from other recently published laboratory studies and other measurements at the SLTEST site [Mathis et al. (2009a), Metzger et al. (2007)]. The data of Fig. 3-13 indicate that λ_u/δ is smaller at low Reynolds numbers. This finding is qualitatively consistent with earlier observations [Hutchins & Marusic (2007)]. The trend of the present low δ^+ data causes these data to nominally merge with the other measurements on the plot. Overall, Fig. 3-13 indicates that λ_u/δ attains a value of about 6 by $\delta^+ \simeq 7,000$, but then apparently decreases to a value closer to 3 at higher δ^+. There is, however, significant uncertainty in the measurement of the wavelength at which Ψ_u is a maximum. As noted previously, the present high Reynolds number estimate is believed to be low owing to the limited range

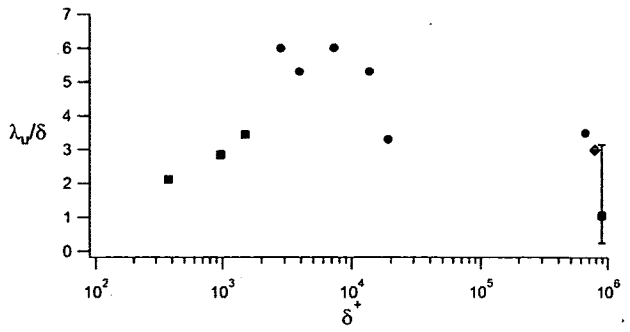

Figure 3-13. λ_u/δ values from Fig. 3-12 where the profiles level-off (horizontal lines): present data, ■; Mathis et al., [Mathis et al. (2009a)] ●; Metzger et al., [Metzger et al. (2007)] ♦. Error bar on the high Reynolds number data point represents the full data scatter of the underlying ensemble.

of measurements beyond layer III and, more importantly, the diminished spectral resolution of these measurements at large wavelengths. In this regard, it is perhaps relevant to note that the recent analysis of data from the SLTEST site by Guala et al. [Guala et al. (2011)] places the plateau value at $\lambda_u/\delta \simeq 1.2$.

Figure 3-14a plots λ_v^+ profiles versus y^+. Comparison of these profiles with those in Fig. 3-12a reveals that λ_v^+ behaves differently (both qualitatively and quantitatively) than λ_u^+. In this plot, each of the low δ^+ profiles exhibit a near wall peak that moves outward in y^+ units with increasing δ^+. Similarly, each profile attains a minimum value farther from the wall that also moves outward when measured in y^+ units. Beyond this minimum, all of the low δ^+ profiles exhibit a monotonic ($\sim$ power law) increase out to the edge of the boundary layer. The spectral resolution of Ψ_v at high δ^+ is much better than for Ψ_u, and although more limited, the high Reynolds number λ_v^+ data also convincingly display this monotonic trend. These data are, however, shifted significantly upward. This upward shift is shown below to be consistent with the small but discernible increase in the low Reynolds number profiles with increasing δ^+. A power law fit of the high Reynolds number data is included on Fig. 3-14a.

The low Reynolds number profiles of Fig. 3-14a exhibit the remarkable attribute that at $y = \delta$ the average streamwise wavelength of the $v(t)$ motions is equal to δ, i.e., in Fig. 3-14a $\lambda_v^+ = \delta^+$ at $y^+ = \delta^+$. To explore whether this holds at higher Reynolds numbers, the curve-fit of Fig. 3-14a was extrapolated to $y^+ = \delta^+ = 8.9 \times 10^5$. The validity of this extrapolation requires that the monotonic power law-like increase persists in layer IV over the given δ^+ range. As indicated in Fig. 3-14b, this extrapolated value exhibits close agreement with the low δ^+ trend. Overall, the data of Fig. 3-14b are well-approximated by $\lambda_v(\delta) \simeq \delta$.

Figures 3-15a,b explore Reynolds number dependencies relative to the layer structure of Fig. 1-1. Under the $y/\sqrt{\nu\delta/u_\tau} = y^+/\sqrt{\delta^+}$ wall-normal coordinate the near-wall peaks in the profiles of Fig. 3-14a nominally occur at fixed normalized position in Fig. 3-15a. Conversely, the minimum values in the profiles now move slightly inward under this normalization. This behavior is similar to that exhibited by the $v\omega_z$ correlation lengths of Figs. 3-4a-d. In connection with this, the onset of the monotonic power law-like dependence appears to occur at decreasingly smaller values of $y/\sqrt{\nu\delta/u_\tau}$ with increasing δ^+, and, in particular, moves inward of the outer edge of layer III (vertical dashed line).

For $y^+/\sqrt{\delta^+} \geq 2.6$, the profiles of Fig. 3-15a exhibit a clear Reynolds number dependence. Applying the same procedure used to generate the data plotted in Fig. 3-13 yields Fig. 3-15b, which quantifies δ^+ dependence along the outer edge of layer III. As indicated by the curve-fit, these data exhibit a dependence close to $\sqrt{\delta^+}$.

Taken together, Figs. 3-14 and 3-15 indicate that in layer IV λ_v^+ exhibits a power-law dependence on y^+. The starting value for λ_v^+ on this domain is Reynolds number dependent (about equal to $8.8\sqrt{\delta^+}$), while the outer-normalized ending value is given by $\lambda_v/\delta \simeq 1$ independent of Reynolds number. Thus, the end points of the domain are moving apart like $\delta^+ - C\sqrt{\delta^+}$, where C is a constant. Examination of Table 1.1

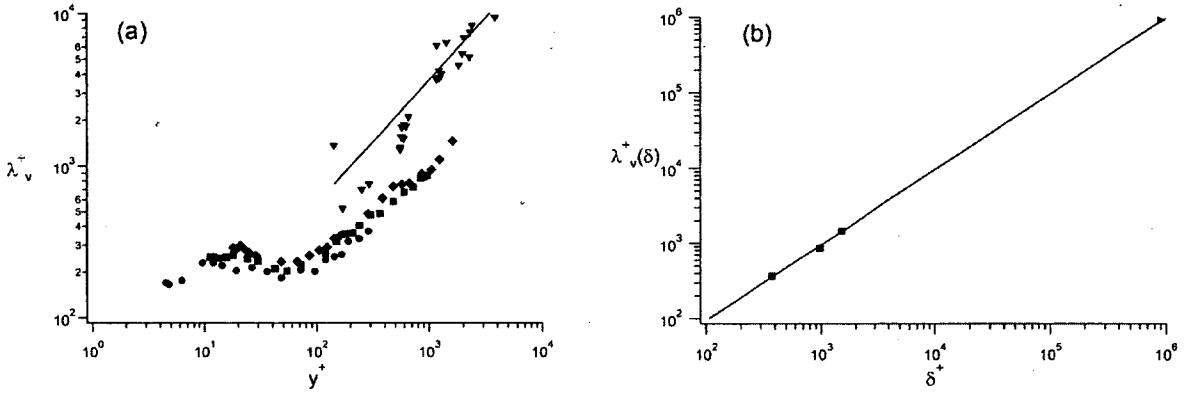

Figure 3-14. Inner-normalized wavelengths at which Ψ_v attains its maximal values. (a) profile versus y^+, $\lambda_v^+(y^+) = 13.57(y^+)^{0.81}$ —. Symbols same as in Fig. 2-1. (b) evaluated at $y = \delta$, low δ^+ measurements, ■; high δ^+ value estimated via extrapolation of the curve-fit in (a), ▶; $\lambda_v^+(\delta^+) = 1.005\delta^+$ —.

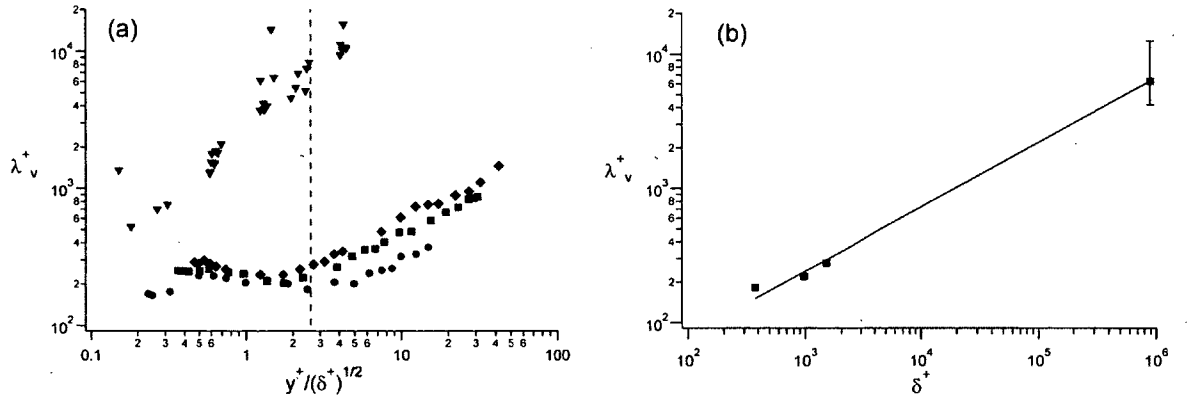

Figure 3-15. Inner-normalized wavelengths at which Ψ_v attains its maximal values. (a) profile versus $y^+/\sqrt{\delta^+}$. Symbols same as in Fig. 2-1. (b) evaluated at $y^+/\sqrt{\delta^+} = 2.6$ and plotted versus δ^+, ■; $\lambda_v = 8.77(\delta^+)^{0.48}$ —. Error bar on the high Reynolds number data point represents the full data scatter of the underlying ensemble.

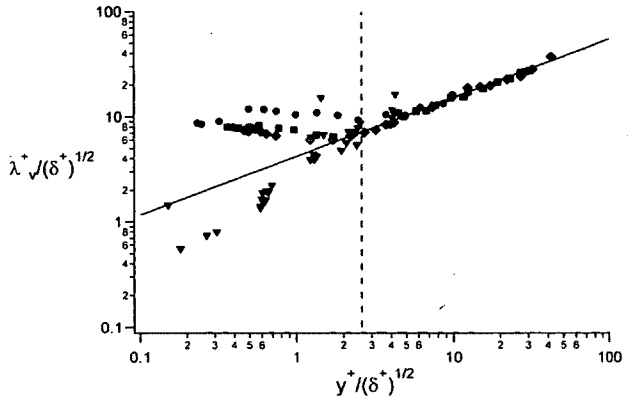

Figure 3-16. Wavelengths at which Ψ_v attains its maximal values normalized by $\sqrt{\nu\delta/u_\tau}$ and plotted versus $y/\sqrt{\nu\delta/u_\tau}$, $\lambda_v^+/\sqrt{\delta^+} = 4.22(y^+/\sqrt{\delta^+})^{0.56}$ —. Symbols same as in Fig. 2-1.

reveals that this is precisely the δ^+ dependence exhibited by the width of layer IV. These behaviors are depicted graphically in Fig. 3-16, by plotting $\lambda_v^+/\sqrt{\delta^+}$ versus $y^+/\sqrt{\delta^+}$. As can be seen, the data in this plot apparently fall on a single line for $y^+/\sqrt{\delta^+} \gtrsim 2.6$. Note also that with increasing δ^+ the laboratory data peel away from this line at decreasing $y^+/\sqrt{\delta^+}$ values, and consistent with the decreasing position of the minimum values in Fig. 3-15a, the data appear to track a power law to positions interior to $y^+/\sqrt{\delta^+} = 2.6$ as δ^+ increases. (Recall that Fig. 3-14a reveals that these minima move outward under inner normalization.) As anticipated from the profiles in Fig. 3-15a, the curve-fit of the data in this figure approximately adheres to a square root dependence on the intermediate coordinate. For $y^+/\sqrt{\delta^+} \gtrsim 1$, the high Reynolds number measurements coincide with the low Reynolds number data. For $y^+/\sqrt{\delta^+} \lesssim 1$, these data fall below the power law line. This feature is distinct from the low δ^+ data. Overall, the data of Fig. 3-16 exhibit the same scaling behavior as the correlation lengths in Fig. 3-4c. Together, these results suggest that the v motions dictate $\overline{v\omega_z}$ in layer IV, which is also consistent with the scale selection data of Figs. 3-8c and d.

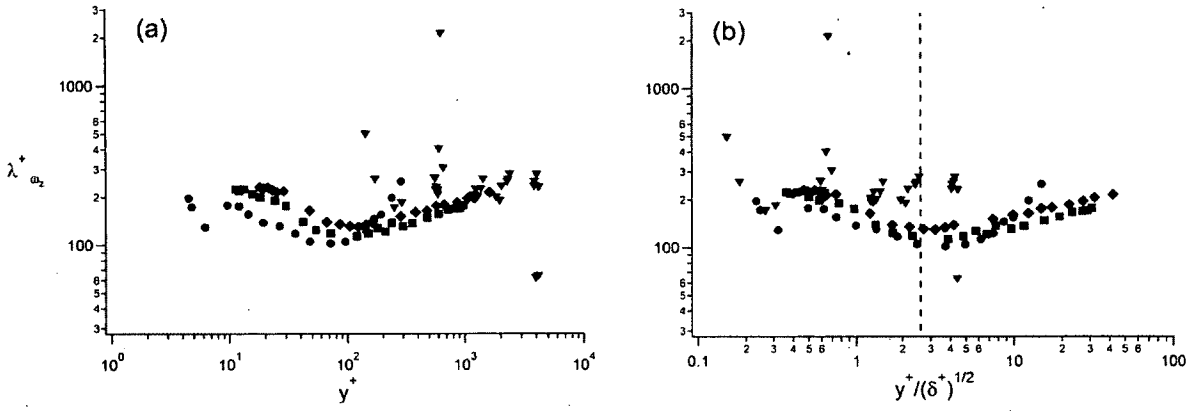

Figure 3-17. Wall-normal profiles of the inner-normalized wavelengths at which Ψ_{ω_z} attains its maximal values; (a) versus y^+, (b) versus $y^+/\sqrt{\delta^+}$. Symbols same as in Fig. 2-1.

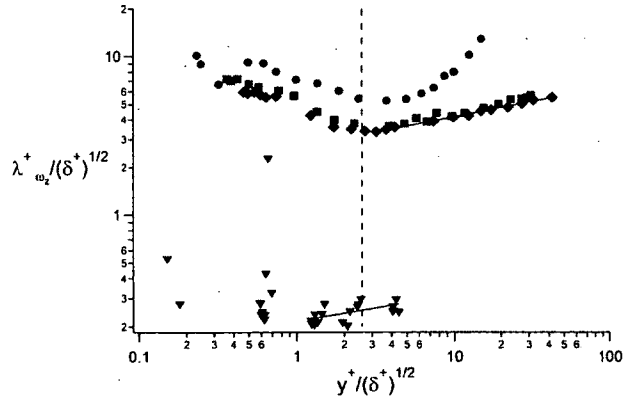

Figure 3-18. Wavelengths at which Ψ_{ω_z} attains its maximal values normalized by $\sqrt{\nu\delta/u_\tau}$ and plotted versus $y/\sqrt{\nu\delta/u_\tau}$. Curve-fits of the high an low δ^+ data have slopes of 0.166 and 0.194 respectively. Symbols same as in Fig. 2-1.

Results pertaining to the wavelengths of the streamwise spectra of the spanwise vorticity fluctuations are shown in Figs. 3-17 and 3-18. Features of the profiles in Figs. 3-17a,b are similar to those observed for λ_v^+. The $\lambda_{\omega_z}^+$ profiles increase with increasing Reynolds number, and exhibit a near-wall maximum. Outward from there they decrease to a minimum. Like the λ_v^+, under inner-normalization (Fig. 3-17a) both the near-wall peaks and the minima move outward with increasing δ^+, and when y is normalized by $\sqrt{\nu\delta/u_\tau}$ (Fig. 3-17b) the near-wall peaks appear to align, while the minima move inward. These results are in accord with the findings of Fig. 3-4b. For y locations greater than the positions of the minima the profiles increase monotonically out to $y = \delta$. The rate of this increase, however, is significantly smaller than exhibited by the λ_v^+ profiles.

Figure 3-16 provides evidence that, for a sub-domain extending from near the position of the interior minimum outward to $y = \delta$, normalization by $\sqrt{\nu\delta/u_\tau}$ causes the profiles of λ_v^+ at different δ^+ to fall on a single curve. This and other features are explored relative to λ_{ω_z} in Fig. 3-18. As clearly indicated, the $\sqrt{\delta^+}$ normalization over-compensates for the increase in $\lambda_{\omega_z}^+$ shown in Fig. 3-17b, and, in fact, this rate of increase is slower than $(\delta^+)^{1/4}$. The data of Fig. 3-18 also provide clear evidence that the minimum in λ_{ω_z} moves from near $y^+/\sqrt{\delta^+} = 4$ at $\delta^+ = 375$ to a little more than $y^+/\sqrt{\delta^+} = 1$ at $\delta^+ \simeq 8.9 \times 10^5$. This is similar to the behavior exhibited by λ_v. This position of minimum wavelength may have connection to the results from recent analyses of axial velocity measurements derived from a vertical rake of hotwires at the SLTEST site. Namely, Guala et al. [Guala et al. (2011)] concluded that the portion of the flow modulated in the manner described by Mathis et al. [Mathis et al. (2009a)] predominantly resides below $y^+ \simeq 1000$, which corresponds to $y^+/\sqrt{\delta^+} \simeq 1.06$ in the present flow. It is similarly worth noting that their results also indicate that the modulation effect is clearly strongest in the region $y^+ \lesssim 40$ (see their Fig. 18), which

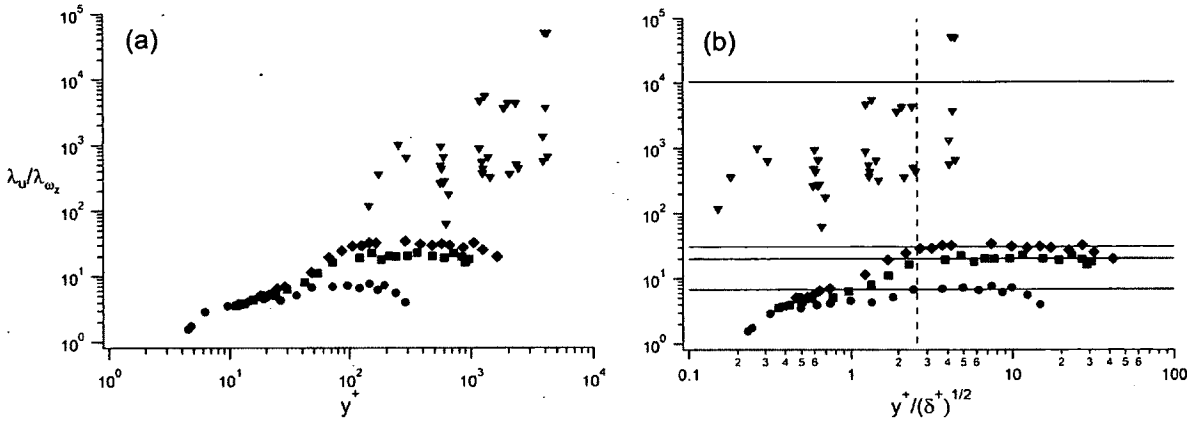

Figure 3-19. Profiles of the $\lambda_u/\lambda_{\omega_z}$ ratios. (a) versus y^+, (b) versus $y^+/\sqrt{\delta^+}$. Symbols same as in Fig. 2-1.

is in close agreement with the correlation length scaling results of Figs. 3-4 and 3-7 herein. The data in Fig. 3-18 also provide evidence that λ_{ω_z} exhibits something close to a weak power law increase with y in layer IV.

The previous figures in this section document the individual behaviors of λ_u, λ_v, and λ_{ω_z}. This facilitates an understanding of how the streamwise scales of the motions respectively affiliated with the u, v and ω_z fluctuations vary across the boundary layer, while normalizations using ν/u_τ, δ, and $\sqrt{\nu\delta/u_\tau}$ allow these wavelengths and their variations to be assessed relative to the minimum, maximum, and mean scales of the L_β hierarchy layer width distribution, $W(y^+)$. Per the Introductory discussion, however, the *intrinsic* scale separations between the relevant components of the overall motion at a point are more aptly quantified by the ratios $\lambda_u/\lambda_{\omega_z}$ and $\lambda_v/\lambda_{\omega_z}$.

Figures 3-19a,b present $\lambda_u/\lambda_{\omega_z}$ versus y^+ and $y^+/\sqrt{\delta^+}$, respectively. Overall, these data reveal significant and clarifying features that are not as readily discerned from either Figs. 3-12 or 3-17. The data of Fig. 3-19a provide a clear indication that the three low δ^+ profiles merge under inner normalization for $y^+ \lesssim 30$. This figure also shows that as the wall is approached $\lambda_u/\lambda_{\omega_z}$ approaches unity. (Note that the no-slip boundary condition enforces an exact correspondence between the $u(t)$ and $\omega_z(t)$

signals as $y \rightarrow 0$, see discussion pertaining to Fig. 3-1b.) Outside of the region of where the profiles merge, each profile shows an increase. This is distinct from the data of Fig. 3-12, as the $\delta^+ = 375$ profile of λ_u^+ remains nearly constant. The ratio of Figs. 3-19a,b increases in this region owing to the more dramatically decreasing values of λ_{ω_z}. In either case, the results of Figs. 3-12 or 3-19 reveal that at the onset of the four layer regime ($\delta^+ \simeq 360$) there is very little scale separation between the motions in layers II and IV.

With increasing Reynolds number, however, the scale separation between the motions characteristic of u and ω_z increases with distance from the wall, and then levels-off. The data of Fig. 3-19b show this more distinctly than do the data of Fig. 3-12b. Namely, the values in the plateau region exhibit less variation, and, at each of the laboratory Reynolds numbers, this plateau convincingly begins at the onset of layer IV. Furthermore, the estimated values of $\lambda_u/\lambda_{\omega_z}$ at $y^+/\sqrt{\delta^+} = 2.6$ apparently exhibit a more well-defined Reynolds number trend, although the scatter of $\delta^+ \simeq 8.9 \times 10^5$ data remains large. The data of Fig. 3-20 indicates that in layer IV the scale separation between the streamwise wavelengths of u and ω_z increases in proportion to δ^+. Note, however, that the remarkable alignment exhibited by the high δ^+ data point with the low δ^+ trend is believed to be at least partly fortuitous. This is because the average value represented in Fig. 3-20 derives from an ensemble with a couple of very large values, see Fig. 3-19a,b.

The profiles of $\lambda_v/\lambda_{\omega_z}$ versus y^+ and $y^+/\sqrt{\delta^+}$ are respectively shown in Figs. 3-21a,b. For a region near the wall, the low δ^+ data are nearly constant and only slightly greater than 1.0. This is distinct from the behavior of $\lambda_u/\lambda_{\omega_z}$, where values approaching 1.0 are only found near layer I. Beyond this region, the low δ^+ profiles show reasonable agreement and exhibit an approximate power law increase with a slope of about 0.4. Somewhat remarkably, even at $\delta^+ = 1,500$ the motions

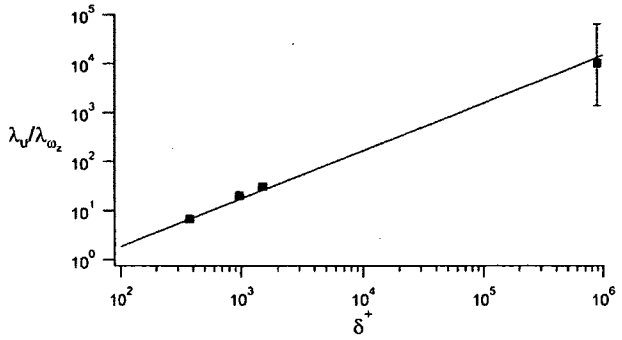

Figure 3-20. $\lambda_u/\lambda_{\omega_z}$ values evaluated at $y^+/\sqrt{\delta^+} = 2.6$ (vertical line in Fig. 3-19b). Curve-fit given by $\lambda_u/\lambda_{\omega_z} = 0.02(\delta^+)^{0.98} \simeq \delta^+/60$. Error bar on the high Reynolds number data point represents the full data scatter of the underlying ensemble.

attributable to the peak in Ψ_v are at most only about 6 times larger than those attributable to the peak in Ψ_{ω_z}. The high Reynolds number data in Fig. 3-21a appear to overlap with those at low Reynolds number, but have a considerably different slope.

As might be anticipated from the individual behaviors of λ_v^+ and $\lambda_{\omega_z}^+$ (Figs. 3-15 and 3-17), the $y^+/\sqrt{\delta^+}$ coordinate employed in Fig. 3-21b results in a convincing alignment of the knee of the low Reynolds number profiles. This change in slope occurs near $y^+/\sqrt{\delta^+} = 1$. The high Reynolds number data are distinctly above the low δ^+ profiles, but are trending toward 1.0 as $y^+/\sqrt{\delta^+} \to 0$. (Note that at $\delta^+ \simeq 8.9 \times 10^5$, $y^+ = 10$ corresponds to $y^+/\sqrt{\delta^+} \simeq 0.01$.) Given the reasonably well-behaved scaling behaviors exhibited by the λ_v^+ profiles under this normalization, we surmise that the distinctly different profiles at high and low Reynolds numbers occur owing to the somewhat perplexing Reynolds number variations in λ_{ω_z}. That is, from Figs. 3-18 and 3-21b it is rational to speculate that over some relatively small Reynolds number range between $1,500 \leq \delta^+ \leq 8.9 \times 10^5$ there is a rapid change in the relationship between the v and ω_z motions.

For completeness, the ratios of λ_u/λ_v are presented in Figs. 3-22a,b. Consistent with the combination of effects indicated in Figs. 3-12a and 3-14a, these profiles

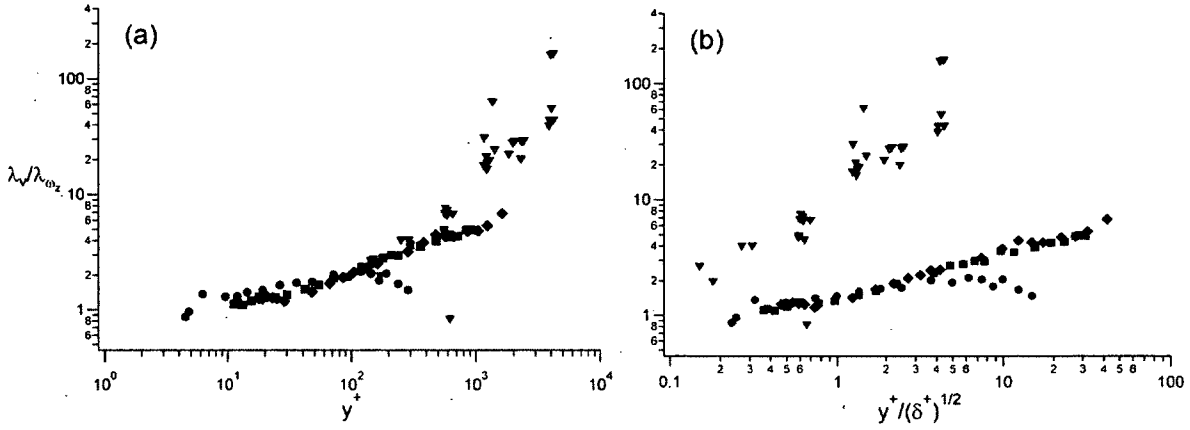

Figure 3-21. Profiles of the $\lambda_v/\lambda_{\omega_z}$ ratios. (a) versus y^+, (b) versus $y^+/\sqrt{\delta^+}$. Symbols same as in Fig. 2-1.

show an increasingly distinct peak at $y/\sqrt{\nu\delta/u_\tau} = 2.6$. On each side of this peak the profiles decrease to minimum values near $y^+ = 0$ and $y/\delta = 1$. The power law fit of the peak values from the laboratory data shown in Fig. 3-22b exhibits a dependence slightly less than directly proportional to δ^+. As can be seen, however, the $\delta^+ \simeq 8.9 \times 10^5$ are highly scattered and exhibit a mean value much less than predicted by the low δ^+ fit. Once again, much of this discrepancy can be attributed to the poor resolution of the large wavelengths of the u spectrum. On the other hand, if the trends indicated by the laboratory data persist for all higher δ^+, then the peak of the profiles of Fig. 3-22a would not asymptote as $\delta^+ \to \infty$, while the end points would remain $O(1)$. This is rationally questionable on physical grounds, and thus higher δ^+ data that accurately captures the large wavelengths is required to clarify this issue. The data of Fig. 3-22a do, however, clearly indicate that the maximum scale separation between λ_u and λ_v is convincingly attained at the outer edge of layer III.

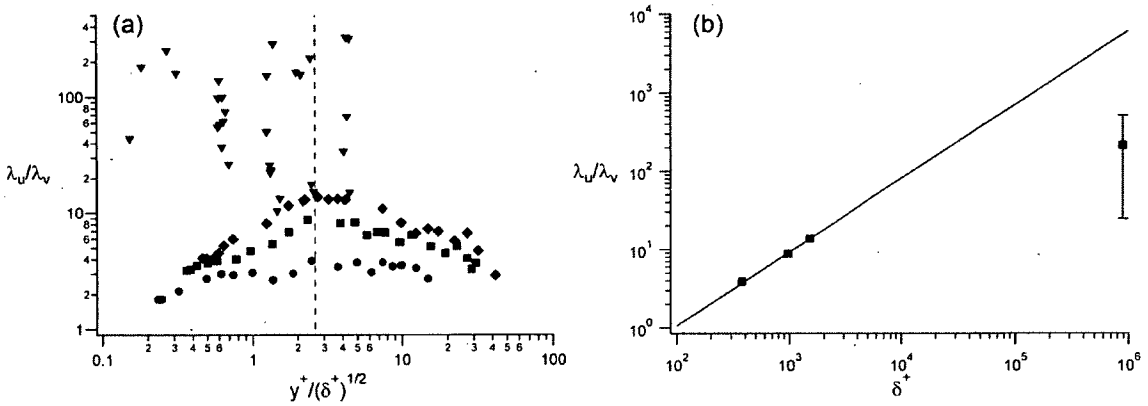

Figure 3-22. Profiles of the ratio λ_u/λ_v, (a) versus $y^+/\sqrt{\delta^+}$, (b) values at $y^+/\sqrt{\delta^+} \simeq 2.6$ versus δ^+. Fit of the low δ^+ data is given by $\lambda_u/\lambda_v = 0.014(\delta^+)^{0.94}$. Symbols same as in Fig. 2-1.

CHAPTER 4

CONCLUSIONS AND DISCUSSION

Physical interpretations of the present data were provided in the discussions of the individual results. Thus, in this section we summarize the primary conclusions, and briefly discuss some of their broader implications.

The theoretical framework described at the outset proved useful in characterizing the present data trends. The high Reynolds number data in Fig. 2-1 provide evidence that the outer peak in u'^{+} occurs where the VF term loses dominant status in (1.7). The characteristic lengths affiliated with $R_{v\omega_z}$ are shown to adhere to the theoretical expectations in Figs. 3-4c,d. Similarly, the data of Figs. 3-15 show that λ_v scales like $\sqrt{\delta^+}$ at the onset of layer IV, while the evidence in Fig. 3-16 suggests that outward from there λ_v follows the theoretically determined scaling for layer IV. (In connection with this, evidence was provided indicating that $\lambda_v(\delta) \simeq \delta$ independent of δ^+, Fig. 3-14b.) The inner-normalized streamwise wavelengths corresponding to the peaks in the u spectra plateau at a fixed value near the outer edge of layer III (Fig. 3-12b). This correspondence becomes much more apparent when the intrinsic scale separation, as quantified by $\lambda_u/\lambda_{\omega_z}$, is plotted versus $y/\sqrt{\nu\delta/u_\tau}$ (Fig. 3-19b). At the outer edge of layer III, and thus across layer IV, the magnitude of this ratio appears to increase in proportion to δ^+ (Fig. 3-20). This is in accord with layer IV scaling. The low δ^+ profiles of $\lambda_v/\lambda_{\omega_z}$ exhibit nearly perfect alignment when plotted versus $y/\sqrt{\nu\delta/u_\tau}$ (Fig. 3-21b). This is the scaling theoretically determined to be affiliated with the TI term in (1.7).

Scale separation occurs as a function of both wall-normal position and Reynolds number. Overall, the present results support the existence of two types of scale separation between the velocity and vorticity spectra. Near the wall, there is a region where the λ_{ω_z} decreases in scale, and especially so when compared to λ_u. At all but the lowest δ^+, this region is confined to within layer II. The scale separation in this region is affiliated with the spatial confinement of the vorticity field and is attributed to vortex stretching, especially in the region between the onset of the L_β hierarchy ($y^+ \simeq 7$) and $y^+ = 40$. As mentioned previously, this region contains highly straining motions in the x, y plane, and is marked by an inverse energy cascade [Klewicki & Falco (1996), Saikrishnan et al. (2012)]. The latter of these is likely to be associated with the spatial organization of the near-wall vorticity field by larger scale outer region motions. Starting near layer III, λ_{ω_z} increases in scale, but much more slowly than λ_v. The scale separation from this point outward is affiliated with the spatial dispersion of the narrow regions of high vorticity over the layer IV domain. Physical evidence of this process was first given by the measurements of Meinhart and Adrian [Meinhart & Adrian (1995)] which show that the outer region of the boundary layer is characterized by zones of nearly uniform momentum that are segregated by narrow vortical fissures. Priyadarshana et al. [Priyadarshana et al. (2007)] provide an interpretation of how such motions can lead to the scale selection phenomena observed in the $v\omega_z$ cospectrum.

At low Reynolds numbers near the wall, scale selections associated with the positive and negative peaks in the $v\omega_z$ cospectrum are difficult to discern, since the peaks in Ψ_v and Ψ_{ω_z} nearly coincide (Fig. 3-8). For the high δ^+ data, the scale separation is large, and the near-wall data in this case provide evidence of scale selections with the peaks in both Ψ_v and Ψ_{ω_z} (Fig. 3-9). With increasing distance from the wall, both the high and low Reynolds number data indicate the existence of a strong scale

selection with Ψ_v. This shift to a velocity dominated scale selection in layer IV is consistent with the correlation length scaling of Fig. 3-4d, and the λ_v scaling shown in Fig. 3-16. The data of Figs. 3-10 and 3-11 consistently indicate that regions of negative $\partial q^+/\partial y^+$ correlate with a negative peak in the $u\omega_z$ cospectrum near the peak in Ψ_{ω_z} and a positive cospectrum peak near the peak in Ψ_u.

The correlation length scale analyses depicted in Figs. 3-4 and 3-7 reveal important results regarding the influences on the near-wall flow caused by motions larger than $O(\nu/u_\tau)$. The results of Fig. 3-4b provide evidence that the over the domain $7 \lesssim y^+ \lesssim 40$ the magnitudes of the $R_{v\omega_z}$ correlation lengths scale with $\sqrt{\nu\delta/u_\tau}$. Examination of the underlying correlations further reveal that normalization of Δx by $\sqrt{\nu\delta/u_\tau}$ aligns both the major peaks and tails of $R_{v\omega_z}$ at essentially all measured y^+ locations. Regarding these observations, the results from the present high Reynolds number data provide evidence that for some $\delta^+ > 1500$ a change occurs in the relationship between the motions bearing v and those bearing ω_z. It is speculated that this may have connection to a mixing transition, in which the organized vortical motions abruptly develop a more complex and intermittent internal structure at sufficiently high δ^+ [Dimotakis (2000), McKeon & Morrison (2004)]. Other comparisons of fine scale structure between laboratory and field data provide similar evidence [Metzger (2006)].

The results of Fig. 3-7b show that in the region $y^+ < 40$ the $R_{u\omega_z}$ correlation lengths scale on δ when plotted versus y^+, but beyond this region increase at a rate that out-paces the growth of δ – at least over the range $375 \leq \delta^+ \leq 1500$. In this near-wall region, the individual correlations show evidence of being characterized by two predominant length scales. The major peaks in the $R_{u\omega_z}$ at small Δx appear to scale on $\sqrt{\nu\delta/u_\tau}$, while the tails of the correlations appear to best scale with δ. Farther away from the wall, there is more tentative evidence that the peaks near

$\Delta x = 0$ scale with δ. The tails of the correlations for $y^+ \gtrsim 40$ out-pace the growth rate of δ.

The correlation length scale analyses provide rather clear evidence that a primary element of the inner-outer interaction is that motions greater than $O(\nu/u_\tau)$ strongly influence the spatial organization of the vorticity field in the region $y^+ \leq 40$. For the motions associated with the TI term in (1.7) the characteristic scale of the perturbation is $O(\sqrt{\nu\delta/u_\tau})$. For the motions associated with $\partial q^+/\partial y^+$ the characteristic scale of the perturbation is $O(\delta)$. These observations are likely to have direct connections with the modulation phenomena recently revealed by Mathis et al, [Mathis et al. (2009a)] as well as the previous and recent evidences that large scale streamwise accelerations have a deterministic influence on the processes associated with near-wall vorticity transport [Hutchins et al. (2011), Wei & Willmarth (1989), Klewicki (1997)].

BIBLIOGRAPHY

[Klewicki (2010)] J. Klewicki, "Reynolds number dependence, scaling, and dynamics of turbulent boundary layers," J. Fluids Eng., **132**, 094001 (2010).

[Marusic et al. (2010)] I. Marusic, B. J. McKeon, P. A. Monkewitz, H. M. Nagib, A. J. Smits, and K. R. Sreenivasan, "Wall-bounded turbulent flows: Recent advances and key issues," Phys. Fluids, **22**, 065103 (2010).

[Klewicki (1989a)] J.C. Klewicki, "Velocity-vorticity correlations related to the gradients of the Reynolds stress in parallel turbulent wall flows," Phys. Fluids A, **1**, 1285 (1989).

[Lele (1992)] S.K. Lele, "Vorticity form of turbulence transport equations," Phys. Fluids A, **4** 1767 (1992).

[Eyink (2008)] G. Eyink, "Turbulent flow in pipes and channels as cross-stream 'inverse cascades' of vorticity," Phys. Fluids, **20**, 125101 (2008).

[Wei et al. (2005)] T. Wei, P. Fife, J. Klewicki and P. McMurtry, "Properties of the mean momentum balance in turbulent boundary layer, pipe and channel flows," J. Fluid Mech., **522**, 303 (2005).

[Long & Chen (1981)] Long and Chen, "Experimental evidence for the existence of the mesolayer in turbulent systems," J. Fluid Mech., **105**, 19 (1981).

[Afzal (1982)] N. Afzal, "Fully developed turbulent flow in a pipe: An intermediate layer," Ing.-Arch., **52**, 355 (1982).

[Sreenivasan & Sahay (1997)] K. Sreenivasan and A. Sahay, "The persistence of viscous effects in the overlap region and the mean velocity in turbulent pipe and channel flows," in *Self-Sustaining Mechanisms of Wall Turbulence*, edited by R. Panton, Computational Mechanics Publications, Southampton, 253 (1997).

[Elsnab et al. (2011)] J. Elsnab, J. Klewicki, D. Maynes & T. Ameel, "Mean dynamics of transitional channel flow," J. Fluid Mech., **678**, 451 (2011).

[Klewicki et al. (2011)] J. Klewicki, R. Ebner & X. Wu, "Mean dynamics of transitional boundary layer flow," J. Fluid Mech., **682**, 617 (2011).

[Klewicki et al. (2012)] J. Klewicki, C. Chin, H. Blackburn, A. Ooi & I. Marusic, "Emergence of the four layer dynamical regime in turbulent pipe flow," Phys Fluids, in press (2012).

[Klewicki et al. (2007)] J. Klewicki, P. Fife, T. Wei and P. McMurtry, "A physical model of the turbulent boundary layer consonant with mean momentum balance structure," Phil. Trans. Roy. Soc. A, **365**, 823 (2007).

[Fife et al. (2005)] P. Fife, J. Klewicki, P. McMurtry & T. Wei, "Multiscaling in the presence of indeterminacy: Wall-induced turbulence," Multiscale Modeling and Simulation, **4**, 936 (2005).

[Fife et al. (2009)] P. Fife, J. Klewicki and T. Wei, "Time averaging in turbulence settings may reveal an infinite hierarchy of length scales," J. Discrete and Contin. Dyn. Syst., **24**, 781 (2009).

[Klewicki et al. (2009)] J. Klewicki, P. Fife and T. Wei, "On the logarithmic mean profile," J. Fluid Mech., **638**, 73 (2009).

[Wu and Moin (2009)] X. Wu and P. Moin, "Direct numerical simulation of turbulence in a nominally zero-pressure-gradient flat-plate boundary layer," J. Fluid Mech., **630**, 5 (2009).

[Townsend (1976)] A. A. Townsend. *The Structure of Turbulent Shear Flow.* Vol.2, Cambridge University Press, (1976).

[Perry & Chong (1982)] A. E. Perry and M.S. Chong, "On the Mechanism of Wall Turbulence," J. Fluid Mech., **119**, 173 (1982).

[Perry & Marusic (1995)] A. E. Perry and I. Marusic, "A wall-wake model for the turbulence structure of boundary layers. Part 1. Extension of the attached eddy hypothesis," J. Fluid Mech., **298**, 361 (1995).

[Metzger & Klewicki (2001)] M.M. Metzger and J.C. Klewicki, "A comparative study of wall region structure in high and low Reynolds number turbulent boundary layers," Phys. Fluids, **13**, 692 (2001).

[DeGraaff & Eaton (2000)] D.B. DeGraaff and J.K. Eaton, "Reynolds number scaling of the flat plate turbulent boundary layer," J. Fluid Mech., **422**, 319 (2000).

[Hutchins & Marusic (2007)] N. Hutchins and I. Marusic, "Large scale influences in near-wall turbulence," Phil. Trans. Roy. Soc. Lond. A, **365**, 647 (2007).

[Mathis et al. (2009a)] R. Mathis, N. Hutchins, and I. Marusic. "Large-scale amplitude modulation of the small-scale structures in turbulent boundary layers," J. Fluid Mech., **628**, 311 (2009).

[Mathis et al. (2009b)] R. Mathis, J. Monty, N. Hutchins, and I. Marusic, "Comparison of large-scale amplitude modulation in turbulent boundary layers, pipes, and channel flows," Phys. Fluids, **21**, 111703 (2009).

[Nagib et al. (2007)] H. Nagib, K. Chauhan, and P. Monkewitz. "Approach to an asymptotic state for zero pressure gradient turbulent boundary layers," Phil. Trans. Roy. Soc. Lond. A, **365**, 755 (2007).

[Tennekes & Lumley (1972)] H. Tennekes and J. Lumley. *A First Course in Turbulence.* MIT Press, Cambridge (1972).

[Smits et al. (2011)] A. Smits, B. McKeon, and I Marusic, "High Reynolds number wall turbulence," Ann. Rev. Fluid Mech., **43**, 353 (2011).

[Hutchins et al. (2011)] N. Hutchins, J.P. Monty, B. Ganapathisubramani, H.C.H. Ng and I. Marusic, "Three-dimensional conditional structure of a high-Reynolds-number turbulent boundary layer," J. Fluid Mech., **673**, 255 (2011).

[Priyadarshana et al. (2007)] P. Priyadarshana, J. Klewicki, S. Treat, and J. Foss, "Statistical structure of turbulent-boundary-layer velocity-vorticity products at high and low Reynolds numbers," J. Fluid Mech., **570**, 307 (2007).

[Klewicki (1998)] J. Klewicki, "Connecting vortex regeneration with near-wall stress transport," AIAA paper no. 98-2963(1998).

[Monty et al. (2011)] J.P. Monty, J.C. Klewicki and B. Ganapathisubramani "Characteristics of momentum sources and sinks in turbulent channel flow," in Proc. *Turbulent Shear Flow Phenomena 7* paper no. IC4P (2011).

[Klewicki et al. (1995)] J. Klewicki, M.M. Metzger, E. Kelner and E.M. Thurlow, "Viscous sublayer flow visualizations at $R_\theta \simeq 1,500,00$," Phys. Fluids, **7**, 857 (1995).

[Klewicki et al. (1998)] J.C. Klewicki, J.F. Foss and J.M. Wallace, "High Reynolds number $[R_\theta = O(10^6)]$ boundary layer turbulence in the atmospheric surface layer above western Utah's salt flats," in *Flow at Ultra-High Reynolds and Rayleigh Numbers*, edited by R.J. Donnelly and K.R. Sreenivasan, Springer, New York, 450 (1998).

[Klewicki & Falco (1990)] J. Klewicki and R. Falco, "On accurately measuring statistics associated with small scale structure in turbulent boundary layers using hot-wire probes," J. Fluid Mech., **219**, 119 (1990).

[Klewicki & Falco (1996)] J. Klewicki and R. Falco, "Spanwise vorticity structure in turbulent boundary layers," Int. J. Heat and Fluid Flow, **17**, 363 (1996).

[Priyadarshana & Klewicki (2004)] P. Priyadarshana and J. Klewicki, "Study of the motions contributing to the Reynolds stress in high and low Reynolds number turbulent boundary layers," Phys. Fluids, **16**, 4586 (2004).

[Sadr & Klewicki (2000)] R. Sadr and J. Klewicki, "Surface shear stress measurement system for boundary layer flow over a salt playa," Meas. Sci. and Tech., **11**, 1403 (2000).

[Johansson & Alfredsson (1983)] A. Johansson and P. Alfredsson, "Effects of imperfect spatial resolution on measurements of wall-bounded turbulent shear flows," J. Fluid Mech., **137**, 409 (1983).

[Antonia et al. (1993)] R. Antonia, Y. Zhu and J. Kim, "On the measurement of lateral velocity derivatives in turbulent flows," Expts. Fluids, **15**, 65 (1993).

[Hutchins et al. (2009)] N. Hutchins, T. Nickels, I. Marusic and M. Chong, "Hot-wire spatial resolution issue in wall-bounded turbulence," J. Fluid Mech., **635**, 103 (2009).

[Folz & Wallace (2009)] A. Folz and J.M. Wallace, "Near-surface turbulence in the atmospheric boundary layer," Physica D, **239**, 1305 (2009).

[Ragagopaln & Antonia (1993)] S. Ragagopalan and R.A. Antonia, "Structure of the velocity field associated with the spanwise vorticity in the wall region of a turbulent boundary layer," Phys. Fluids A, **5**, 2502 (1993).

[Klewicki (1989b)] J. Klewicki, *On the interactions between the inner and outer region motions in turbulent boundary layers.* PhD Dissertation, Michigan State University, East Lansing, MI (1989).

[Metzger et al. (2007)] M. Metzger, B.J. McKeon and H. Holmes, "The near-neutral atmospheric surface layer: Turbulence and non-stationarity," Phil. Trans. R. Soc. Lond. A, **365**, 859 (2007).

[Guala et al. (2011)] M. Guala, M. Metzger and B.J. McKeon, "Interactions within the turbulent boundary layer at high Reynolds number," J. Fluid Mech., **666**, 573 (2011).

[Saikrishnan et al. (2012)] N. Saikrishnan, E. De Angelis, E.K. Longmire, I. Marusic, C.M. Casciola and R. Piva, "Reynolds number effects on scale energy balance in wall turbulence," Phys. Fluids, **24**, 015101 (2012).

[Meinhart & Adrian (1995)] C.D., Meinhart and R.J. Adrian, "On the existence of uniform momentum zones in a turbulent boundary layer," Phys. Fluids, **7**, 694 (1995).

[Dimotakis (2000)] P.E., Dimotakis, "The mixing transition in turbulent flows," J. Fluid Mech., **409**, 69 (2000).

[McKeon & Morrison (2004)] B.J. McKeon and J.F. Morrison, "The mixing transition and inertial scaling in fully-developed pipe flow," in Proc. *Second International Workshop on Wall-bounded Turbulent Flows*, Trieste, Italy (2004).

[Metzger (2006)] M.M. Metzger, "Length and time scales of the near-surface axial velocity in a high Reynolds number turbulent boundary layer," Int. J. Heat and Fluid Flow, **27**, 57 (2006).

[Wei & Willmarth (1989)] T. Wei and W.W. Willmarth, "Reynolds number effects on the structure of a turbulent channel flow," J. Fluid Mech., **204**, 57 (1989).

[Klewicki (1997)] J.C. Klewicki, "Self-sustaining traits of near-wall motions underlying boundary layer stress transport," in *Self-Sustaining Mechanisms of Wall Turbulence*, edited by R. Panton, Computational Mechanics Publications, Southampton, 135 (1997).